

A *SPITZER* STUDY OF ASYMPTOTIC GIANT BRANCH STARS. III. DUST PRODUCTION AND GAS RETURN IN LOCAL GROUP DWARF IRREGULAR GALAXIES.

Martha L. Boyer¹, Evan D. Skillman², Jacco Th. van Loon³, Robert D. Gehrz², and Charles E. Woodward²

ABSTRACT

We present the third and final part of a census of Asymptotic Giant Branch (AGB) stars in Local Group dwarf irregular galaxies. Papers I and II presented the results for WLM and IC 1613. Included here are Phoenix, LGS 3, DDO 210, Leo A, Pegasus dIrr, and Sextans A. *Spitzer* photometry at 3.6, 4.5, 5.8, and 8 μm are presented, along with a more thorough treatment of background galaxy contamination than was presented in papers I and II. We find that at least a small population of completely optically obscured AGB stars exists in each galaxy, regardless of the galaxy's metallicity, but that higher-metallicity galaxies tend to harbor more stars with slight IR excesses. The optical incompleteness increases for the redder AGB stars, in line with the expectation that some AGB stars are not detected in the optical due to large amounts of extinction associated with in situ dust production. Overall, there is an underrepresentation of 30% – 40% in the optical AGB within the 1σ errors for all of the galaxies in our sample. This undetected population is large enough to affect star formation histories derived from optical color-magnitude diagrams. As measured from the $[3.6] - [4.5]$ color excesses, we find average stellar mass-loss rates ranging from $3.1 \times 10^{-7} - 6.6 \times 10^{-6} M_{\odot} \text{ yr}^{-1}$, and integrated galaxy mass-loss rates ranging from $4.4 \times 10^{-5} - 1.4 \times 10^{-3} M_{\odot} \text{ yr}^{-1}$. The integrated mass-loss rate is sufficient to sustain the current star formation rate in only LGS 3 and DDO 210, requiring either significant non-dusty mass loss or gas accretion in Phoenix, Leo A, Pegasus dIrr, Sextans A, WLM, and IC 1613 if they are to maintain their status as gas-rich galaxies.

Subject headings: dwarf-galaxies: individual (Phoenix, LGS 3, DDO 210, Leo A, Pegasus dIrr, Sextans A, WLM, IC 1613)–galaxies: irregular–Local Group–stars: AGB and post-AGB–stars: carbon–stars: mass loss–stars: formation

1. INTRODUCTION

After a star with mass $0.8 M_{\odot} < M < 8 M_{\odot}$ has exhausted the helium in its core, it will experience a short stay ($\approx 1 - 13$ Myr; Vassiliadis & Wood 1993) on the Asymptotic Giant Branch

¹STScI, 3700 San Martin Drive Baltimore, MD 21218 USA; mboyer@stsci.edu

²Astronomy Department, School of Physics and Astronomy, 116 Church Street, S.E., University of Minnesota, Minneapolis, MN 55455 USA

³Astrophysics Group, School of Physical & Geographical Sciences, Keele University, Staffordshire ST5 5BG, UK

(AGB), where it will burn hydrogen and helium in concentric shells around a degenerate C/O core. During the final 0.2 – 2 Myr of its life, an AGB star will undergo radial pulses, which may allow dust condensation in the circumstellar envelope. Radiation pressure on the dust grains and momentum coupling between the grains and the gas results in the formation of an additional slow, dense wind (Gehrz & Woolf 1971). This wind causes the star to lose 20 – 60% of its mass, truncating its subsequent evolution.

AGB stars are uniquely important to many aspects of galactic and stellar astronomy. Mass-losing AGB stars are the main source of long-term gas return to the interstellar medium (ISM), prolonging the star-formation life of gas-rich galaxies. AGB winds are heavily enriched in Li, C, N, F, and s-process elements, and are the largest source of dust input into the ISM (Gehrz 1989), making AGB stars an important driver of chemical evolution in galaxies. The intermediate masses of AGB stars make them ideal candidates for probing the star formation histories (SFHs) across much of a galaxy’s lifetime. Also, because they are widely distributed and easily detected, AGB stars are excellent tracers of galactic structure. While unobscured AGB stars are among the brightest stars in optical band-passes, they are best studied in the infrared (IR) and the near-IR, where emission from warm circumstellar dust peaks and circumstellar extinction is minimal. However, a lack of sufficient sensitivity and resolution has prevented comprehensive studies in the near-IR and IR in systems other than the Magellanic Clouds (e.g., Loup et al. 1997; Trams et al. 1999; Cioni et al. 2003; Whitelock et al. 2003). While near-IR observations of distant stellar systems remain difficult, the recent launch of the *Spitzer Space Telescope* has overcome most IR observing obstacles.

Dwarf irregular (dIrr) galaxies in the Local Group provide us with ideal laboratories to study AGB stars. Most of these galaxies are undergoing recent or on-going star formation, resulting in a population of AGB stars representative of the entire mass range rather than a snapshot of a single AGB mass. The nearby dwarf irregular galaxies are populous enough to capture a substantial number of AGB stars in the short-lived mass-loss phase, near enough to resolve the stellar population, and distant enough to encompass the entire galaxy with a small field of view. *Spitzer’s* ability to detect the entire AGB population in a given galaxy also provides us with the means to study the mass and dust injection rate into the Interstellar Medium (ISM), the fate of the ISM, and the effect on continued star formation and chemical evolution of the galaxy.

This paper is the third and final part of our *Spitzer* mid-IR IRAC survey of Local Group dIrr galaxies, designed to obtain a complete census of AGB stars. Jackson et al. (2007a) (hereafter paper I), and Jackson et al. (2007b) (hereafter paper II) presented a complete AGB census in WLM and IC 1613, respectively. Here, we present the results for six more Local Group dIrr galaxies and provide a comprehensive summary of the results for all eight galaxies. Our total sample of eight galaxies spans 1 dex in metallicity, allowing us to study AGB dust production and mass loss in metal-poor environments as a function of metallicity. This metallicity range also enables us to investigate the degree to which optical studies of these targets are biased by the inability to detect the entire AGB population due to dust obscuration.

In §2, we describe the observations, data reduction, and ancillary data. We present and describe the IR color-magnitude diagrams (CMDs) in §3 and also discuss the stellar spatial distributions, detection statistics, stellar luminosity, and stellar mass. §4 details a complete census

of the AGB stars in all eight galaxies and estimates of AGB mass-loss rates (MLRs) and ISM gas return. We summarize our results in § 5.

2. OBSERVATIONS AND DATA REDUCTION

2.1. *Sample Selection*

Papers I and II discuss the AGB populations in the Local Group dIrr galaxies WLM and IC 1613, which are very similar in luminosity, gas content, and metallicity. In order to broaden the environments for which we have complete AGB censuses, we have chosen six more Local Group dIrr galaxies for this study: Phoenix dwarf, LGS 3 (Pisces dIrr), DDO 210 (Aquarius dIrr), Leo A (DDO 69), Pegasus dIrr (DDO 216), and Sextans A (DDO 75). Including these six galaxies with WLM and IC 1613 increases the luminosity range to 4.6 mag, the range in H I mass by a factor of 800, and the range in $12 + \log(\text{O}/\text{H})$ to 0.9. See Table 1 for a list of basic galaxy properties.

The angular sizes of the galaxies presented here are small enough to obtain complete coverage, and the galaxies are near enough to resolve stars down to or below the tip of the Red Giant Branch (TRGB), above which mass-losing AGB stars reside. The span in metallicity ($Z \approx 2\% - 19\% Z_{\odot}$; Lee et al. 2006; van Zee et al. 2006), provides us with the opportunity to examine how metal content affects dust production, mass return, and optical completeness (§ 4).

Each galaxy shows some evidence for recent star formation (age < 3 Gyr; Dolphin et al. 2005), providing a large sample of intermediate-aged stars, and consequently, a large sample of AGB stars. LGS 3 has the lowest rate of recent star formation in our sample, followed closely by Phoenix. Sextans A, WLM, and IC 1613 are forming stars at a rate two orders of magnitude higher than LGS 3. A brief summary of the star formation histories from Dolphin et al. (2005) is given in § 3.

2.2. *Infrared Data and Photometry*

New observations were obtained with the Infrared Array Camera (IRAC; Fazio et al. 2004) onboard the *Spitzer Space Telescope* (Werner et al. 2004; Gehrz et al. 2007). The observing program (PID 40524) was designed to image Phoenix, LGS 3, DDO 210, Leo A, and Pegasus dIrr at 3.6 and 5.8 μm . The same five galaxies were also observed earlier at 4.5 and 8 μm as part of a larger guaranteed time observing (GTO) program (PID 128; PI: R. D. Gehrz). Sextans A was observed as part of the GTO program at all four IRAC wavelengths. See Table 2 for a summary of the observations. GTO 4.5 and 8 μm data were observed with a 5-point Gaussian dither pattern (*Spitzer Science Center* 2006) and an exposure time of 193.6 s, yielding a total depth of 968 s. To build a better redundancy against outliers and artifacts while maintaining a similar exposure depth, images obtained as part of PID 40524 were observed with a 36-point reuleaux dither pattern (*Spitzer Science Center* 2006) and exposure time of 26.8 s, for a total depth of 965 s. Sextans A was observed at 3.6 and 5.8 μm as part of PID 128 with a 16-point reuleaux dither pattern and exposure time of 26.8 s, for a total depth of 858 s. For all observations, we used small-scale dither patterns to allow for sub-pixel sampling. These observations yielded 5σ point-source sensitivities of 1.3, 2.3,

15.0, and 17.5 μJy at 3.6, 4.5, 5.8, and 8 μm , respectively. Sextans A 5σ sensitivities are 1.4 μJy at 3.6 μm and 15.9 μJy at 5.8 μm . These sensitivities were computed using the *Spitzer* sensitivity calculator¹ and do not include confusion with other sources. However, since these galaxies are not particularly crowded, confusion is not a major source of uncertainty in the IR flux. The coverage area for all six galaxies is approximately $5.8' \times 5.8'$, centered at the coordinates listed in Table 2. Figure 1 displays the field of view overlaid on the Digitized Sky Survey images of the six selected galaxies.

GTO and PID 40524 IRAC data were processed with pipelines S14.0.0 and S16.1.0, respectively, with the exception of the PID 40524 data for Leo A, which was processed with pipeline S17.0.4. The Basic Calibrated Data (BCD) were reduced and mosaicked with the MOPEX² reduction package (Makovoz & Marleau 2005) after applying an array distortion correction. We implemented the MOPEX overlap routine to match backgrounds between overlapping areas of the images and the MOPEX mosaicker for outlier elimination, image interpolation, and co-addition. The final mosaics have pixel sizes of $0.86'' \text{ pix}^{-1}$ and are presented in Jackson et al. (2006). The 8 μm mosaics are affected by persistent images resulting from observations of very bright objects immediately preceding our program. These artifacts were removed by subtracting a median-combined image from each individual frame before proceeding with MOPEX.

Point-source extraction was performed with the DAOPhot II package (Stetson 1987). PSFs were created from a minimum of 10 isolated stars in each mosaic, and sources 4σ above the background were chosen for extraction. Extended galaxies and outliers that are broader or narrower than the PSF were rejected based on sharpness and roundness cut-offs. The final fluxes are color-corrected (*Spitzer* Science Center 2006) using a 5000 K blackbody, which is an appropriate temperature for a typical Red Giant star. The color correction listed for a 2000 K star in *Spitzer* Science Center (2006) differs by less than 1%. A pixel-phase-dependent correction (Reach et al. 2005) has been applied to the 3.6 μm photometry. Photometric errors include standard DAOPhot errors and the IRAC absolute calibration errors (Reach et al. 2005). Magnitudes relative to α Lyr (Vega) are derived using the zero magnitudes quoted in the *Spitzer* IRAC data handbook (*Spitzer* Science Center 2006). Table 3 shows a sample from the full point-source catalog, which is available electronically and includes IRAC photometry for each of the eight galaxies in our sample.

2.3. Optical Photometry

We used optical data for each galaxy to aid in source classification, which is challenging with IRAC data alone (see §3). Broadband *V* and *I* images of Sextans A, Pegasus dIrr, and Phoenix were obtained from the Local Group Galaxies Survey³ (LGGS; Massey et al. 2006). The LGGS survey nicely complements IRAC data because the coverage includes the entire IRAC field of view,

¹<http://ssc.spitzer.caltech.edu/tools/senspet/>

²MOPEX is available from the *Spitzer* Science Center at <http://ssc.spitzer.caltech.edu/postbcd>

³LGGS data are publicly available at <http://www.lowell.edu/~massey/lgsurvey/>.

and the angular resolution is similar to the IRAC resolution (median seeing $\approx 1''$). The published LGGS photometry only includes sources 10σ above the background, rendering an incomplete CMD. In order to reliably identify different regions of the CMD, it was necessary to recover sources down to 4σ above the background. We performed PSF photometry on the LGGS images ourselves with DAOPHOT II. Precise absolute photometry was not required since the V and I data were used only to identify sources in optical CMDs. We therefore used “stacked” images with relative photometric errors of $\approx 10\%$ instead of photometric images since image processing, including co-addition and astrometric calibration, had already been performed on the former. To calibrate the LGGS magnitude offsets between instrumental and true magnitudes, we compared our photometry to the published LGGS calibrated 10σ photometry lists. The magnitude offsets and color terms were computed using least-squares fitting.

V and I photometry of DDO 210 and Leo A were obtained with the SUBARU telescope by McConnachie et al. (2006) and Vasevicius et al. (2004). As with the LGGS, the SUBARU coverage includes the entire IRAC field of view and the angular resolution is similar to the IRAC resolution ($0.8''$ seeing for both DDO 210 and Leo A). The calibrated photometry lists compiled by McConnachie et al. (2006) for DDO 210 and Vasevicius et al. (2004) for Leo A are sufficiently complete and have relative photometry errors $\lesssim 10\%$.

Optical photometry of LGS 3 was obtained with permission from the Local Cosmology from Isolated Dwarfs Survey (LCID; Gallart 2008), which imaged several Local Group Dwarfs with the ACS camera onboard the *Hubble Space Telescope* (HST) with the F475W and F814W filters. The total optical coverage for ACS is $\approx 3.3' \times 3.3'$ (Fig. 1). The resolution and PSF of the ACS camera is vastly superior to those of IRAC, making cross-correlation between the IR and optical data difficult for LGS 3. To facilitate comparisons between optical and IR photometry of AGB candidates in LGS 3, we inspected the IRAC and ACS images by eye to be sure we found the correct IR counterparts of the 12 optical point sources detected in the HST images above the I -band TRGB. Due to the inferior resolution of IRAC, the identified IR counterparts have potentially been blended with other optical point sources, enhancing the IRAC flux. However, the 12 optical AGB stars span the entire IRAC image, leaving no danger of blending between two or more optical AGBs. The vast majority of the flux from each IR source is therefore originating from the optically-identified AGB star, since other optical sources would contribute only very small amounts of flux in the IR. All optical sub-TRGB sources in LGS 3 remain unmatched to *Spitzer* sources.

2.4. Source Contamination

The main contributors of contamination to the *Spitzer* and optical photometry lists are unresolved background galaxies and foreground stars. We used the Milky Way stellar population synthesis model of Robin et al. (2003) to estimate the degree of contamination in each IRAC field from the latter. Foreground stellar counts for 1 deg^2 fields centered on the Galactic coordinates of each galaxy were generated to reduce statistical error. The Robin et al. (2003) model provides Johnson-Cousins L band magnitudes, which is similar to the IRAC $3.6 \mu\text{m}$ band. In the IRAC coverage area, we expect to find 6 foreground stars in the Phoenix and Leo A mosaics, 10 foreground

stars in the Pegasus dIrr, Sextans A, and LGS 3 mosaics, and 32 foreground stars in the DDO 210 mosaic. These stars are expected to have $[3.6] - [4.5]$ colors near zero and $-6 \lesssim M_L \lesssim -20$. The contamination from foreground stars is therefore only 0.5% – 3.5% of the total number of point sources detected at 3.6 μm . This contamination is reflected in error bars and uncertainties throughout this paper. Background galaxies are a more insidious contamination, accounting for anywhere from 20% – 70% of the sources brighter than the 3.6 μm TRGB and residing in an IRAC color-magnitude locus similar to that of obscured AGB stars. The effect of background contamination on the analyses presented in this paper is discussed in detail in §3.4.

While most of the sources belonging to each galaxy are AGB stars, there may also be a small population of young stellar objects (YSOs). YSOs in the Large Magellanic Cloud (LMC) have typical 8 μm magnitudes of $m_{8.0} \approx 10$ mag and have similar colors to AGB stars, with $2 \lesssim [3.6] - [8.0] \lesssim 4$ (Whitney et al. 2008). At the distance of the LMC, this puts the vast majority of YSOs at $M_{3.6} \gtrsim -6.5$ mag, which is approximately equal to the TRGB of each of the galaxies in our sample (see §3.2.1). Therefore, only the most massive YSOs ($M \gtrsim 5 M_\odot$) are included in our AGB statistics. This contamination is likely very small, given the SFHs of these galaxies.

3. COMPARISON OF OPTICAL AND IR PHOTOMETRY

3.1. *Optical Color-Magnitude Diagrams*

IRAC data sample the Rayleigh-Jeans tail of the Planck function, providing very little information about stellar effective temperatures and making it necessary to identify source types in the optical. Optical CMDs are shown as Hess diagrams in Figure 2. Lines divide the regions where (a) blue objects, (b) AGB stars, (c) red supergiants (RSGs), and (d) red giants (RGs) below the TRGB reside. Sources located in (d) will hereafter be referred to as sub-TRGB stars. The gap widths between the regions reflect the 1σ photometric errors and reduce misidentification solely due to photometric uncertainty. Circumstellar and interstellar reddening can also cause source misidentification that is not corrected for in Figure 2.

The optical CMDs show features that indicate a wide variety of SFHs among these six galaxies. Sextans A shows the strongest evidence for recent and intermediate age star formation with prominent plumes of blue helium burning stars, RSGs, and AGB stars that are consistent with an increase in star formation rate (SFR) by a factor of three 1 Gyr ago and a factor of five 100 Myr ago (Dolphin et al. 2005, 2003b). Leo A also shows a prominent branch of blue helium burning stars, reflecting a twofold increase in the recent SFR over the lifetime average ≈ 1 Gyr ago (Dolphin et al. 2005).

Pegasus dIrr has been forming stars at a moderately high rate over its lifetime, but the SFR has steadily decreased during the last 1 Gyr. Blue stars in DDO 210 suggest some star formation 3 – 6 Gyr ago (McConnachie et al. 2006), and the SFR has remained steady throughout the lifetime of the galaxy (Dolphin et al. 2005). The SFH of Phoenix (Holtzman et al. 2000; Dolphin et al. 2005; Young et al. 2007) reveals that star formation ceased ~ 100 Myr ago. LGS 3 is similar to Phoenix

because it has been forming stars at a low, but constant level since its initial star formation event (Miller et al. 2001; Dolphin et al. 2005), but a lack of blue stars in LGS 3 suggests very little recent star formation.

3.2. IRAC Color-Magnitude Diagrams

The $M_{3.6}$ versus $[3.6] - [4.5]$ CMDs are shown in Figure 3. These CMDs show all sources detected at 3.6 and 4.5 μm along with the photometric errors, averaged over one-magnitude bins. The 50% completeness limits, averaged over the entire fields of view, are also shown as a solid black line. Unlike WLM, none of the galaxies in this sample are particularly crowded in the infrared, so the photometric completeness does not decline significantly toward the centers of the galaxies. Sources that fall along $[3.6] - [4.5] = 0$ sample the Rayleigh-Jeans tail of the Planck function at both 3.6 and 4.5 μm . Other sources are reddened by circumstellar dust emission. The region redward of $[3.6] - [4.5] = 0$ is also populated by background galaxies, although these should mostly fall below the dashed line (see § 3.4).

The $M_{3.6}$ versus $[3.6] - [4.5]$ CMDs of all eight galaxies (including WLM and IC 1613 from papers I and II) are very similar and differ significantly only in the depth of the photometry. Phoenix has the fewest bright, red sources ($M_{3.6} < -8, [3.6] - [4.5] > 0.5$), while WLM, IC 1613, and Sextans A contain the largest number of sources in this region. These magnitudes and colors are consistent with obscured, mass-losing AGB stars (see § 4).

Isochrones from Marigo et al. (2008), computed for single-aged populations of $\log(t) = 8.25$ (black), 8.75 (magenta), and 9.25 (blue) at the metallicity of each galaxy (Table 1), are overlaid on the $M_{3.6}$ versus $[3.6] - [4.5]$ CMDs in Figure 4. These isochrones do not perfectly fit the IR data (e.g., see Figure 3 of Whitelock et al. 2008), but they do offer the best representation to date of IR stellar populations due to the inclusion of dust in the models. The thick lines show the isochrones that do not include dust, and the thin lines show isochrones computed with 60% Silicate + 40% AlO_x for O-stars, and 85% amorphous carbon + 15% SiC for C-stars. It is clear from these isochrones that dusty, mass-losing AGB stars are not only red in color, but are also some of the brightest stars on the CMD. These isochrones are not a good match to faint, red stars ($M_{3.6} \gtrsim -7 \text{ mag}, [3.6] - [4.5] \gtrsim 0.5$). This discrepancy may be due to a combination of photometric uncertainty in this region of the CMD and contamination from other source types, particularly background galaxies.

Figure 5 shows point-sources residing in regions (a), (b), (c), or (d) of the optical CMDs (Fig. 2) of Phoenix, DDO 210, Leo A, Pegasus dIrr, and Sextans A; red squares are red giants, green triangles are optical AGB stars, black stars are RSGs, and blue circles are blue objects. LGS 3 is excluded from Figure 5 due to difficulty in matching the *Spitzer* sources to the ACS sources as discussed in § 2.3. Since there is virtually no extinction at 3.6 μm , we show a vector in the first panel of Figure 5 illustrating the displacement corresponding to 10 magnitudes of visual extinction and the associated reddening (Rieke & Lebofsky 1985; Indebetouw et al. 2005). This vector does not take into account the effect of dust emission, which can be considerable in the infrared. The AGB limit was determined by scaling AGB stars with $T_{\text{eff}} = 2650$ and 3600 K and negligible mass loss

(Groenewegen 2006) to bolometric magnitudes of $M_{\text{bol}} = -7.1$ mag. The lines shown in Figure 5 connect the limits of these two hypothetical stars. AGB stars that are undergoing heavy mass loss can attain $3.6 \mu\text{m}$ fluxes brighter than this limit due to thermal emission from the expelled material. Such stars would also have red $[3.6] - [4.5]$ colors, as is the case for one star in Leo A (Fig. 3). All other stars above the AGB limit in our galaxy sample are likely RSGs. Note that few of the stars following the isochrones in Figure 4 are detected in the optical, especially in Leo A. Moreover, of those stars that are detected in V and I , many are not *optically* identified as AGB stars and are either contaminants or obscured AGB stars.

3.2.1. The Tip of the Red Giant Branch

Figure 5 also shows the locations of the $3.6 \mu\text{m}$ TRGB. The TRGB was identified by plotting the luminosity functions of stars detected at both 3.6 and $4.5 \mu\text{m}$ (Fig. 6) and determining the magnitude where the source count decreases significantly. We adopt TRGB values of $M_{3.6} = -6.38 \pm 0.25$, $M_{3.6} = -5.88 \pm 0.25$, $M_{3.6} = -6.13 \pm 0.25$, $M_{3.6} = -5.88 \pm 0.25$, and $M_{3.6} = -6.38 \pm 0.25$ mag for Phoenix, LGS 3, DDO 210, Leo A, and Pegasus dIrr, respectively. The dotted lines in Figure 6 represent the IR luminosity function of sub-TRGB stars identified in the optical. In each case, the number counts of the sub-TRGB stars support what we have determined is the location of the TRGB. Sub-TRGB stars that are brighter than the $3.6 \mu\text{m}$ TRGB have very red colors that are consistent with heavily obscured, mass-losing AGB stars and might be reddened enough in the optical to be misidentified as sub-TRGB.

The IRAC photometry of Sextans A is not deep enough to reliably determine the $3.6 \mu\text{m}$ TRGB, but the luminosity function of the sub-TRGB stars seems to suggest a TRGB of approximately $M_{3.6} = -6.13$ mag. In papers I and II, we found $3.6 \mu\text{m}$ TRGBs of $M_{3.6} = -6.6 \pm 0.2$ mag for WLM and $M_{3.6} = -6.2 \pm 0.2$ mag for IC 1613. Most of our values are a few tenths of a magnitude fainter than the TRGB found in the LMC ($M_{3.6} = -6.65$ mag; Blum et al. 2006), but this discrepancy is not necessarily unexpected since different SFHs will yield different TRGBs due to varying ages and metallicities of RGB stars. The $3.6 \mu\text{m}$ TRGBs in old star clusters in the Magellanic Clouds is $M_{L'} \approx -6$ mag (van Loon et al. 2005), which is more consistent with the TRGB values measured here.

3.2.2. $8 \mu\text{m}$ Color-Magnitude Diagrams

The $M_{8.0}$ versus $[4.5] - [8.0]$ CMD is presented in Figure 7. In these CMDs, sources below the $3.6 \mu\text{m}$ TRGB are plotted as open circles. As with Figure 3, this CMD is similar for all eight galaxies. The main features are a narrow plume centered at $[4.5] - [8.0] = 0$ and a bright, red plume with $M_{8.0} < -8.0$ mag and $[4.5] - [8.0] > 1.0$. The red plume is strongly populated in all eight galaxies, with the exception of Phoenix, which has fewer than 10 stars in this region that are brighter than the TRGB. Based on the colors of background galaxies in ω Cen (Boyer et al. 2008), the reddest regions of the CMDs in Figure 7 are contaminated by background galaxies ($[4.5] - [8.0] > 2$), although the most heavily obscured AGB stars can also reach colors as red as

$[4.5] - [8.0] \approx 5$.

Isochrones for two different ages are overlaid in Figure 7 (≈ 0.5 and 2 Gyr; Marigo et al. 2008) and demonstrate that obscured AGB stars are bright at $8 \mu\text{m}$. Because the isochrones appear to be systematically bluer than the data, we do not attempt a fit, but it is clear that the locus of the bright, red plume of sources in each galaxy is consistent with obscured AGB stars, while fainter red sources may be other source-types such as background galaxies or YSOs.

3.3. *Detection Statistics*

The detection statistics for the regions shared by optical and IRAC photometry are presented in Table 5 (note that the LGS 3 optical coverage is smaller than the IR coverage due to the small field of view of the ACS camera). We consider a source to be detected in V and I only if it is brighter than $M_I = -2.5$ mag, which is the approximate limiting magnitude of the shallowest optical data. Sextans A has the largest $8 \mu\text{m}$ population, followed by Pegasus dIrr. The number of detections in the IRAC data of IC 1613 and WLM presented in papers I and II are much higher than all six of the galaxies presented here, but that is due to an increased areal coverage (more IRAC fields) rather than to an intrinsic property of the galaxies themselves.

In each galaxy, we find between 27 – 67 sources that are detected in all four IRAC bands, but not in V and I . The majority of these sources lie between the TRGB and the AGB limit and may be either optically obscured AGB stars or background galaxies. We are unable to determine the corresponding numbers for LGS 3 due to the difficulty of matching IRAC data to ACS data (see § 2.3). However, we have inspected the bright optical sources by eye and note that there are a mere 12 stars brighter than the I -band TRGB in LGS 3 that are also detected in IRAC. For comparison, in the IRAC images, there are 102 sources located between the $3.6 \mu\text{m}$ TRGB and the AGB limit in LGS 3 in the area covered by the ACS data.

A small number of the IRAC detections with no optical counterparts are above the AGB limit and have colors near zero. These bright sources are probably foreground stars or RSG stars, as any AGB star above the AGB limit would have a very red color.

There is strong evidence for confusion by background galaxies in our sample (see § 3.4), especially below the $3.6 \mu\text{m}$ TRGB. Phoenix, the nearest of the eight galaxies in our sample, hosts the largest number of sources that are below the $3.6 \mu\text{m}$ TRGB and not detected in the optical (25 sources total; Table 5). The region occupied by background galaxies in Figure 3 is at the faintest absolute magnitude for Phoenix, pushing many of the background galaxies below the $3.6 \mu\text{m}$ TRGB. As a result, Phoenix has the smallest number of background galaxies *above* the TRGB at $3.6 \mu\text{m}$.

3.4. *Background Galaxy Contamination*

Unresolved background galaxies tend to have $[3.6] - [4.5]$ colors very similar to optically obscured AGB stars. Based on inspection of IRAC CMDs alone, background galaxies are easily identified in observations of nearby stellar populations such as the Magellanic Clouds (Blum et al.

2006; Bolatto et al. 2007) and ω Centauri (Boyer et al. 2008) because the AGB stars in these nearby systems have far brighter apparent magnitudes than the background objects. Unfortunately, the distances to our target dIrr galaxies are just large enough so that dusty AGB stars and unresolved background galaxies occupy the same color-magnitude space and are impossible to disentangle, potentially causing an overestimate of the dust production and integrated mass-loss rate in each galaxy. Because WLM and IC 1613 have the highest stellar surface densities in the sample, the effects of unresolved background galaxies were more subtle and not dealt with in papers I and II. The lower stellar surface densities of the galaxies in the new sample makes the effects of unresolved background galaxies more obvious, and thus we can address these effects in this study.

In the *Spitzer* observations of ω Centauri (Boyer et al. 2008), the unresolved background galaxies remained confined to $3.6 \mu\text{m}$ apparent magnitudes fainter than ≈ 16 mag and colors $-0.3 \gtrsim [3.6] - [4.5] \lesssim 1.0$. This limit suggests that we may be confident that any red point-sources brighter than $m_{3.6} = 16$ mag are mass-losing AGB stars. Below this limit, we cannot distinguish between mass-losing AGB stars, background galaxies, and other red IR sources (e.g., YSOs) with IRAC data alone. It is clear in Figure 3 that the pack of red sources fainter than $m_{3.6} = 16$ mag has a similar shape in each galaxy and slides up and down with respect to the rest of the IR population, depending on the distance to the galaxy. Phoenix, which is the nearest galaxy in our sample, is the least affected by contamination since the background galaxy limit is only one magnitude brighter than the TRGB. In Sextans A, on the other hand, the region occupied by galaxies reaches up to 3.5 mag brighter than the TRGB.

In fact, if we assume that the background galaxy populations in the images of Phoenix, LGS 3, DDO 210, Leo A, Pegasus dIrr, and Sextans A are the same (the IRAC images for these six galaxies have the same areal coverage), we should find approximately the same number of sources fainter than $m_{3.6} = 16$ mag and redder than $[3.6] - [4.5] \approx 0$. We created Hess diagrams with 0.1 mag color bins and 0.5 mag magnitude bins for Figure 3 and subtracted the Phoenix Hess diagram from the others, since the Phoenix background population is the least mixed with real AGB stars. We find that, in the region of contamination, the subtraction leaves only ± 10 sources in each bin, suggesting that the majority of sources in this region of the CMD are in fact background galaxies.

In order to obtain a first-order estimate of the degree of contamination above the TRGB in each of our targets, we inspected the IRAC CMDs produced with photometry from the *Spitzer*-Cosmic Evolution (S-COSMOS) database (Sanders et al. 2007), which is a *Spitzer* Legacy survey covering a 2 deg^2 dark portion of the sky. S-COSMOS is complete to more than one magnitude below the $3.6 \mu\text{m}$ TRGB of our most distant galaxy, allowing a direct comparison of the background galaxies in S-COSMOS to the number of and distribution of sources above the TRGB in each galaxy in our sample. We applied the distance modulus of each galaxy to the S-COSMOS CMD and counted sources with magnitudes brighter than the TRGB and $[3.6] - [4.5]$ colors redder than 0.2. After correcting for the field size, we find that background galaxies may account for anywhere from 21% to 50% of the sources brighter than the $3.6 \mu\text{m}$ TRGB (Table 5).

For targets that lie in the direction towards a large galaxy cluster, the galaxy counts can be significantly larger. LGS 3 and IC 1613 are each located within $30'$ from the center of one galaxy cluster and Leo A and WLM are each located within $30'$ from the centers of two such clusters (see

Table 4 for a list of galaxy clusters within 1 degree of our targets; Abell 1995; Fernandez et al. 1996). None of these clusters are particularly large or heavily populated, but their presence could potentially double the number of background galaxies above the average population. Moreover, LGS 3 is projected onto the fringes of the Pisces-Pegasus Supercluster of galaxies, which may cause an even larger increase in the background galaxy counts in the LGS 3 images.

In order to measure the background galaxy contamination directly from the data, a large field of view is necessary. A search of the *Spitzer* archive revealed IRAC off-fields for Phoenix, DDO 210, Leo A, and Pegasus dIrr as part of the Large Volume Legacy Survey (Kennicutt et al. 2007), but the depth of these observations is less than 20% the depth of our observations, preventing reliable photometry of sources down to the TRGB.

Figures 8 and 9 display the spatial distributions of IR sources with (*right*) and without (*left*) optical counterparts. While not completely avoiding the central parts of each galaxy, IR sources without optical counterparts are more numerous on the outskirts, where unresolved background galaxies are expected to begin to dominate the source counts. Despite the small fields of view of the galaxies in our sample, it is clear from Figures 8 and 9 that background galaxies do, sometimes significantly, contaminate the IR source count. We attempt to measure the contribution from background galaxies in each of our targets using the radial density profiles, a task that would be more robust given a larger field of view but that nonetheless provides interesting results with the available data.

Radial density profiles of sources with and without optical counterparts and brighter than the TRGB are shown in Figure 10, with the latter population normalized to the former. The profiles were determined by placing ellipsoidal annuli on each galaxy at semi-major axis intervals of $0.5'$. We have assumed that the radial profiles should have similar shapes, and that any deviation is due to a flat contribution from background galaxies. Leo A shows the largest difference between the profiles, as might be expected considering the number of background galaxy clusters in that direction (Table 4). DDO 210 shows the flattest overall distribution, which suggests that, for this galaxy, there may be significant contamination in the optical as well as the infrared.

Using a least squares fitting routine, we have fit a combination of a declining profile (the profile for AGB candidates with optical counterparts) plus a flat distribution (background galaxies) to the profile of AGB candidates without optical counterparts. The resulting fits agree with the predictions from S-COSMOS to within 25% for four galaxies (Phoenix, Leo A, Pegasus dIrr, and WLM), 40% for three (LGS 3, DDO 210, and Sextans A), and 78% for IC 1613. The resulting total background contamination for the galaxies in our sample ranges from 25% to 67% of the sources above the TRGB (compared to 21% – 50% from S-COSMOS). For DDO 210, the fit has increased the number of galaxies predicted by S-COSMOS by 37%, resulting in a larger number of background galaxies than there are optical AGB stars. This suggests that either there are no obscured AGB stars in DDO 210, or that DDO 210 is significantly contaminated in the optical, as well as in the infrared.

3.5. *Stellar Spatial Distributions*

The spatial distributions of different stellar types are displayed in Figures 11 and 12. From left to right, the panels show the optically-identified red giant stars, AGB stars, and blue objects, followed by the IR-identified AGB star candidates, which we define as any object between the TRGB and the AGB limit that is not identified as an RSG or a blue object in the optical (§ 4). The analogous figure in paper I for WLM shows the effects of crowding, illustrated by a deficit of fainter red giants in the regions densely populated with blue stars (i.e., the regions containing the youngest stellar populations). Similar crowding is not seen in IC 1613 (Paper II) nor in any of the six other galaxies presented here due to a combination of a lower density of stars and smaller inclination angle (each galaxy, aside from WLM, has $i < 55^\circ$; Mateo 1998, and references therein). It is clear from Figures 11 and 12 that the IRAC data do not cover the entire areal spans of all six galaxies since the stellar densities are still decreasing at the edges of the coverage.

The few IR AGB candidates detected in Phoenix span a similar area to their optically-identified counterparts. Red giants and blue objects in Pegasus dIrr and DDO 210 trace a line from east to west across the fields of view, but the IR AGB candidates are more smoothly distributed. The brightest IR AGB candidates (red circles) in both galaxies tend to cluster more towards the center. Sextans A shows a mildly clumpy structure with the IR AGB candidates loosely tracing the young blue objects and RGB stars. Optical studies of the spatial distributions of the stellar populations are available from HST studies of Pegasus dIrr (Gallagher et al. 1998) and Sextans A (Dohm-Palmer et al. 1997, 2002). In Pegasus dIrr, the youngest stars are strongly clumped, while the AGB stars tend to follow the distribution of the RGB stars. In Sextans A, again, the youngest stars are strongly clumped, but the RGB stars are both centrally concentrated and form a smooth halo-like population. Neither the optically identified nor IR AGB stars in Figure 12 tend to be concentrated in the bar feature. This is consistent with the expectation that the AGB stars show spatial distributions intermediate between those of the youngest and oldest stellar populations.

For LGS 3, it is difficult to draw connections between the distributions of the different stellar types due to the small optical coverage. However, in LGS 3, the distribution of IR AGB candidates is generally smooth across the entire IRAC field of view, with no increase in the number of sources in the regions of highest stellar density. This distribution supports the claim made in § 3.4 that LGS 3 is strongly contaminated by background galaxies. However, even the brightest IR AGB candidates ($m_{3.6} < 16$ mag), marked with red circles in Figure 11, span the entire LGS 3 coverage, suggesting that AGB stars have a broader distribution than the Red Giant Branch (RGB) stars. Leo A, which is also potentially strongly contaminated by background galaxy clusters, has a slightly higher density of IR AGB candidates on the west edge of the field, which is offset from the centers of the blue object and optical red giant distributions. None of the known background galaxy clusters (Table 4) are located near this overdensity. The brightest AGB candidates in Leo A are more broadly distributed (red circles). In both Leo A and LGS 3, the broad distributions of AGB stars are not likely to be a reflection of the true distributions, but rather the result of low number statistics in these lightly populated galaxies. However, we note a recent study of variable stars in the Fornax dwarf galaxy (Whitelock et al. 2008) that suggests that AGB stars in that galaxy are more broadly distributed than the bulk population.

3.6. *Luminosity Contribution from Super-TRGB Stars*

The total fluxes measured from all point sources detected at both 3.6 and 4.5 μm are listed in Table 5. To avoid including bright foreground stars, sources brighter than an apparent magnitude of $m_{3.6} = 14$ mag are excluded from the total flux unless they are optically identified as an AGB or RSG star or have colors $[3.6] - [4.5] > 0.3$. The 3.6 μm flux values quoted here tend to be higher than the integrated 4.5 μm fluxes presented in Lee et al. (2006) and Jackson et al. (2006), which include only the optical and near-IR extent of each galaxy instead of the entire 3.6 and 4.5 μm IRAC coverage. The flux estimates presented here are, of course, overestimates, as they do not exclude the contribution from background galaxies.

In Table 5, we also compare the summed flux of sources one magnitude above the TRGB to that of one magnitude below the TRGB. Choosing to compare the relative fluxes within narrow magnitude intervals directly above and below the TRGB makes this approach less susceptible to the effects of magnitude-dependent completeness and contamination (from galaxies). We find that, in general, this ratio is higher for galaxies with more recent star formation. This correlation confirms that older stellar populations have fewer high-luminosity stars. DDO 210 and Sextans A do not follow the trend, but this is due to incompleteness within one magnitude below the TRGB, since these galaxies are the most distant. LGS 3 is the only other galaxy that does not follow the trend; this may be due to a combination of photometric incompleteness and low number counting statistics.

3.7. *Derived Stellar Mass*

As discussed in the previous section, the number of super-TRGB stars decreases as a galaxy ages, so that the older the stellar population, the higher the underlying stellar mass represented by each super-TRGB star. Following this premise, the van Loon et al. (2005) prescription for determining the total stellar mass of a galaxy based on the number of stars brighter than the TRGB in the L' -band (3.76 μm) yields stellar masses ranging from $5.5 \times 10^5 - 1.2 \times 10^7 M_{\odot}$ (Table 6), assuming an age of 2 Gyr for the current super-TRGB population and excluding estimates of the numbers of background galaxies from S-COSMOS and foreground stars from Robin et al. (2003). These masses are uncertain because they are determined using a single age population and because of incomplete sky coverage in some galaxies. If we adjust the age to coincide with past star formation events (see §3), we find a wider range of stellar masses (Table 6). Because of the assumption of a single-aged stellar population, our mass estimates, with the exception of the estimates for Pegasus dIrr and WLM, are somewhat larger than, but are still within reasonable agreement to, those found by Lee et al. (2006) from the mass-to-metallicity relation.

4. THE AGB STARS

It is important to determine if photometric incompleteness affects our AGB statistics. Photometry in Phoenix, LGS 3, DDO 210, Leo A, and Pegasus dIrr is 50% complete to more than

one magnitude fainter than the TRGB for the reddest sources. The location of the Sextans A TRGB is unknown, but assuming it is near $M_{3.6} = -6.1$ mag (dotted line in Fig. 6), the Sextans A 50% completeness limit is ≈ 0.4 mag fainter than the TRGB for the reddest sources. The bluest sources are 50% complete down to $\gtrsim 0.3$ mag less than the TRGB in Phoenix, LGS 3, DDO 210, Leo A, and Pegasus dIrr. Photometry of the bluest sources in Sextans A is not complete down to $M_{3.6} = -6.1$ mag. Therefore, without considering the very small number of objects not detected due to crowding, our data represent a complete census of super-TRGB stars in the central $5.8' \times 5.8'$ regions of the sampled galaxies, with the exception of the bluest super-TRGB stars in Sextans A. Note that because the least massive AGBs are also the least luminous, barely reaching luminosities exceeding the TRGB (McDonald et al. 2009), we have underrepresented AGB stars from the first epoch of star formation.

4.1. Optical Completeness

After subtracting background galaxies (from S-COSMOS), we detect 37 – 478 IR AGB candidates in the six galaxies discussed in this paper (Table 6). Using the same criteria for defining an AGB candidate, which are slightly different from the criteria used in papers I and II, IC 1613 and WLM contain 594 and 451 AGB candidates, respectively. Of these candidates, 35% – 100% are detected in the optical, *above the I-band TRGB*. While larger percentages are detected in the optical below the *I*-band TRGB, these sources would have been misidentified in the optical and excluded from AGB star studies, thus we define the optical completeness fraction as the fraction of AGB candidates in the IR that are correctly identified in the optical (Table 6). The equivalent percentages in IC 1613 and WLM are not presented in papers I and II, but are computed here to be 79% and 63%, respectively.

Figure 13 shows the metallicity versus optical completeness fractions after correcting for background contamination, as determined from fitting the IR radial profiles (§ 3.4). The error bars reflect the fitting uncertainties, which are largely due to the small fields of view. We have adopted $12 + \log(\text{O}/\text{H})$ values from van Zee et al. (2006), and used the luminosity-metallicity (L - Z) relationship from Lee et al. (2006) to estimate $12 + \log(\text{O}/\text{H})$ for Phoenix, DDO 210, and LGS 3, all of which have no H II regions. No trend with metallicity is apparent in Figure 13, and it is clear that an optical completeness fraction of roughly 60% – 70% is consistent within the errors in all eight galaxies. The AGB in optical surveys is therefore underrepresented by $\approx 35\%$, which may have important consequences for SFHs derived from isochrone fitting to optical CMDs.

In Figure 14, we show the fraction of optical completeness (as defined in this paper) as a function of $[3.6] - [4.5]$ color. The optical extinction (A_V) is shown in the lower right panel. The optical completeness declines as a function of color, approaching 0% for the reddest sources, as expected if the incompleteness is due to circumstellar extinction. For DDO 210, Pegasus dIrr, Sextans A, WLM, and IC 1613, the completeness fraction approaches zero roughly between $0.5 < [3.6] - [4.5] < 1.0$. In Phoenix, LGS 3, and Leo A, the completeness approaches 0% at bluer colors ($[3.6] - [4.5] \approx 0.25$), which is due to the small populations of very dusty AGB stars and to strong background galaxy contamination in these galaxies. Background galaxies are particularly red objects and thus drop

out of the optical at fairly blue colors compared to dusty AGB stars.

As discussed in §3.4, the IR AGB candidate populations are heavily contaminated by background galaxies, and the same trend of decreasing optical completeness with IR color is also consistent with this contamination. Based on fits to the stellar radial profiles, Pegasus dIrr, Sextans A, and WLM have the smallest percentage background galaxy contamination in the IR AGB candidate population. It is interesting to note that two of these three low-contamination galaxies are the only two galaxies in our sample that do not show a sudden drop in completeness near $0.1 < [3.6] - [4.5] < 0.2$, and in the case of Pegasus dIrr, the drop occurs at an intermediate color ($[3.6] - [4.5] \approx 0.3$). This may suggest that at the $[3.6] - [4.5] = 0.1 - 0.2$ color transition, background galaxies become the dominate source type. In galaxies that show a drop in completeness beyond this color transition, there may be few, if any, *very red* AGB stars.

Figure 15 shows the fraction of IR AGB candidates *with* optical counterparts (i.e., *not* background galaxies) that have $[3.6] - [4.5] > 0.2$. The trend in Figure 15 suggests a scarcity of very red AGB stars in some galaxies in our sample. With the exception of DDO 210, there is a clear correlation between metallicity and the fraction of red stars, as expected if dust is produced more efficiently in environments that are rich in metals.

An alternate interpretation of Figure 15 is that stellar populations older than ≈ 3.0 Gyr are unable to produce many stars with $[3.6] - [4.5] > 0.2$, regardless of metallicity (Marigo et al. 2008). The galaxies with the smallest fraction of their current stellar population formed within the last 3 Gyr (Orban et al. 2008) are indeed the galaxies with the fewest very red stars, with the exception of DDO 210.

It is generally assumed that lower metallicity systems will be less dusty than their higher-metallicity counterparts, resulting in a smaller population of dust-enshrouded AGB stars. This is indeed what we see in Figure 15. This should lead to a trend of decreasing optical completeness with increasing metallicity. Nevertheless, we see no convincing correlation between optical completeness and metallicity in Figure 13, suggesting that even environments with very low metallicity ($Z < 2\% Z_{\odot}$, assuming $Z_{\odot} = 0.0122$; Asplund et al. 2004) are capable of forming at least a few heavily enshrouded stars. This is the case even if the majority of the stars in these galaxies harbor little to no dust at all, either due to low metallicity or to an older stellar population.

This result supports an increasing number of observations suggesting that dust formation is not prohibited at low metallicity (Cannon et al. 2002; Boyer et al. 2006; Gruendl et al. 2008; Sloan et al. 2008; Lagadec & Zijlstra 2008), although it is forming in smaller quantities (Boyer et al. 2006; McDonald & van Loon 2007; van Loon et al. 2008). It may be that the ability to form dust has little or no dependence on the initial metal-content, rather, nucleosynthesis in the stars themselves and dredge-up in radial-pulsing AGB stars is the dominant source of dust-forming metals in the circumstellar envelope. However, we must emphasize that we do not have metallicity measurements for any individual stars in our sample, and it is therefore possible that the reddest (i.e., dustiest) stars have higher metallicities than the bulk population.

4.2. The Carbon Stars

In addition to the carbon stars in WLM and IC 1613 (Papers I and II), populations of carbon stars are known in three of the galaxies studied here: DDO 210, Phoenix, and Pegasus dIrr. The remaining three galaxies may also contain carbon stars, but to our knowledge no searches have yet been carried out. Given the rough estimates of the C/M ratios below, we might expect at least a handful of carbon stars in LGS 3, Leo A, and Sextans A. Although, since carbon stars require a mass larger than $1 M_{\odot}$ to form, we might expect few, if any, carbon stars in metal-poor, low star forming galaxies like LGS 3.

4.2.1. Phoenix

Phoenix appears to have a very small population of three carbon stars (Da Costa 1994; Menzies et al. 2008). These three stars were identified through spectroscopic measurements. The brightest carbon star (Fig. 16) is a Mira variable with a period of 425 days (Menzies et al. 2008). All three carbon stars in Phoenix have relatively blue $[3.6] - [4.5]$ colors, which may be due to the low metallicity of the galaxy causing a low optical depth in the circumstellar envelope. If all three stars belong to Phoenix, and the remaining 28 IR-identified AGB candidates identified in this work are M-stars, then the C/M ratio for Phoenix is a mere 0.11.

4.2.2. DDO 210

Using the CN/TiO technique with narrowband optical photometry, Battinelli & Demers (2000) found 3 carbon stars in DDO 210, two of which are located within the *Spitzer* coverage and are detected in IRAC. With broadband near-IR photometry, Gullieuszik et al. (2007) found an additional 6 carbon stars, 4 of which are located within our *Spitzer* coverage and are detected in IRAC. The two Gullieuszik et al. (2007) stars with the reddest $[3.6] - [4.5]$ colors in Figure 16 appear to be Long Period Variables, typical of mass-losing carbon stars. One other carbon star is quite red, while the remaining three have relatively blue colors, similar to the carbon stars in Phoenix.

Battinelli & Demers (2000) also find 158 M-stars in an $8.2' \times 8.2'$ field. By measuring the density of M-stars on the outskirts of their CCD image, Battinelli & Demers (2000) claim that all 158 M-stars are in the foreground, however a later estimate of the C/M ratio in Battinelli & Demers (2005) using modified a distance and reddening computes a C/M ratio of 0.09 ± 0.08 . Assuming an even distribution of all 158 M-stars, we expect 79 of these stars to fall within our IRAC coverage. In §2.4, we found that only 32 foreground stars are expected in the area covered by our IRAC images. If Battinelli & Demers (2000) overestimated the number of foreground M-stars, we are left with 47 M-stars and 6 carbon stars covered in our IRAC images, yielding a C/M ratio of 0.13. If all of the IR-identified AGB candidates (minus background and foreground contamination) reported here (Table 5) are truly AGB stars belonging to DDO 210, then only 26% of the total IR AGB star population is used to compute this ratio, and it should not be over-interpreted.

4.2.3. Pegasus dIrr

The population of carbon stars in Pegasus dIrr is comparable to the populations found in IC 1613 and WLM. With optical narrowband observations, Battinelli & Demers (2000) find 40 carbon stars in Pegasus dIrr, 35 of which fall inside our IRAC coverage, and 32 of which are detected here (three are undetected due to crowding). The bulk of the carbon stars have relatively blue $[3.6] - [4.5]$ colors (Fig. 16); four are very red, and five are very bright at $3.6 \mu\text{m}$. Pegasus dIrr has the highest metallicity of the galaxies in our sample ($12 + \log(\text{O}/\text{H}) = 7.93$), so it seems less likely that the colors are blue entirely because of a low optical depth, as may be the case for Phoenix and DDO 210. Comparison to Figure 4 shows that the brightest carbon stars in Pegasus dIrr match the 560 Myr population better than the older and younger isochrones, which agrees with the enhanced star formation that occurred just short of 1 Gyr ago (Dolphin et al. 2005).

Assuming a color excess of $E(B-V) = 0.03$, the C/M ratio quoted by Battinelli & Demers (2000) is 0.73, and uses a total of 175 AGB stars in an area roughly twice the size of our IRAC coverage. However, based on the numbers of C-stars and M-stars quoted in Table 6 of Battinelli & Demers (2000), we cannot reproduce the C/M ratio and suspect a typographical error; with their numbers, we recalculate $C/M = 0.50$.⁴ A later modification of the distance and reddening towards Pegasus dIrr adjusts the C/M ratio to 0.62 ± 0.22 (Battinelli & Demers 2005). According to the population synthesis models of Robin et al. (2003) (see § 2.4), Battinelli & Demers (2000) overestimated the contamination of M-stars in the foreground by a factor of ≈ 2.8 . Therefore, assuming the population synthesis model is correct and that the distribution of M-stars is flat, yielding 58 M-stars in the IRAC coverage, we recompute the C/M ratio to be 0.60, well within agreement to the most recent C/M ratio calculated by Battinelli & Demers (2005). This ratio is computed with a total of 93 AGB stars, which is only 34% of the IR AGB candidates reported here.

4.3. Mass-Loss Rates

As in papers I and II, we have estimated the MLRs of the AGB candidates in each galaxy by comparing the IR fluxes to the radiative transfer models of Groenewegen (2006). We linearly interpolated the $[3.6] - [4.5]$ colors onto the Groenewegen (2006) models to estimate the optical depth (τ), which corresponds to a particular IR color given assumptions about the wind composition and stellar effective temperature (T_{eff}). The resulting MLRs were then scaled according to van Loon (2006), where $\dot{M} \propto \tau \psi^{-(1/2)} L^{(3/4)}$, ψ is the dust-to-gas ratio, and L is the stellar luminosity. The dust-to-gas ratio scales as $\psi = \psi_{\odot} 10^{[Fe/H]}$ and $\psi_{\odot} = 0.005$ (van Loon et al. 2005). See Table 7 for the average stellar MLRs and Table 8 for integrated galaxy MLRs.

The integrated and average MLRs computed using the entire population of IR AGB candidates are most certainly overestimates, as 21% – 67% of these populations are background galaxies. For this reason, we have also computed the integrated and average MLRs for only sources that

⁴Private communication with S. Demers has confirmed this recalculation.

have optical counterparts with $M_I < -2.5$ mag. This approach excludes any AGB stars that are obscured in the optical, and thus excludes the stars with the most dust and highest MLRs. To regain some of these interesting sources, we have also computed the integrated MLRs for all sources that either have optical counterparts *or* are brighter than $m_{3.6} = 16$ mag, the approximate cut-off between unresolved background galaxies and AGB stars. These totals are listed in Table 8. We have also computed the integrated MLR by subtracting the contribution from the number of galaxies predicted in the S-COSMOS data, assuming each source has the average MLR. This approach inserts more uncertainty into the resulting integrated MLR since background galaxies can artificially inflate or deflate the average, depending on their (incorrectly-assigned) absolute magnitudes.

The stellar MLR versus bolometric magnitude for each galaxy is shown in Figure 17, assuming a dust composition of 85% AMC + 15% SiC and $T_{\text{eff}} = 3600$ K. We have included in this figure only sources that fall between the $3.6 \mu\text{m}$ TRGB and the AGB limit and are not identified in the optical as an RSG or a blue object. Sources below the background galaxy cut-off at $m_{3.6} = 16$ mag that do not have optical counterparts are plotted in small orange points (except for LGS 3, which is not matched to the optical data); these points represent the population that is likely dominated by background galaxies. Carbon stars are plotted in filled blue circles. We find that the most heavily mass-losing stars are among the most luminous AGB candidates. The maximum MLRs in all eight galaxies are in good agreement with that found in the LMC (van Loon et al. 1999), which is somewhat higher than the classical single-scattering MLR limit predicted by Jura (1984), above which a dusty circumstellar envelope results in multiple scattering of photons (Gail & Sedlmayr 1986). The sources that lie above the single-scattering limit are indeed those with the largest optical depths, as determined from their $[3.6] - [4.5]$ colors.

While the vast majority of the AGB candidates have moderate MLRs ($< 10^{-6} M_{\odot} \text{ yr}^{-1}$), there are a handful of sources in each galaxy, with the exception of Phoenix, that are near or above the classical single-scattering limit (short-dashed line in Figure 17; Jura 1984). The brightest of these have the strongest MLRs and dominate each galaxy’s integrated MLR. A few of these heavily mass-losing sources are also undetected in the optical (orange points) and may prove to be background galaxies. However, in Leo A, Sextans A, WLM, and IC 1613, many of these optically obscured, heavily mass-losing sources (1, 2, 4, and 5 sources, respectively) are brighter than the background galaxy cut-off ($m_{3.6} < 16$ mag), and are likely true obscured AGB stars.

The majority of the AGB candidates are in the superwind phase (van Loon et al. 2005; Girardi & Marigo 2007), i.e., the MLRs exceed the nuclear-burning mass consumption rate (\dot{M}_{nuc} ; long-dashed line in Fig. 17). Mass loss is the dominant evolutionary driver for these stars since they will expel their outer layers before exhausting their nuclear fuel.

The timescale of the AGB superwind phase is short ($\sim 10^6$ yr; van Loon et al. 2005; Girardi & Marigo 2007). If we assume that each galaxy hosts a broad range of AGB star masses, then we may also assume that each AGB star loses an average total of $1.5 M_{\odot}$. Using the mean individual MLRs listed in Table 7 (averaged over all five combinations of dust composition and effective temperature), the superwind timescale we derive ranges from $4 \times 10^5 - 2 \times 10^6$ yr, which agrees well with previous estimates. A consequence of this short timescale is that the integrated MLR of low-mass galaxies

may be highly time-variable, as is the case for star clusters (van Loon et al. 2008; McDonald et al. 2009), and must not be over-interpreted. Within a few million years, a mere handful of new, strongly mass-losing AGB stars may appear in some galaxies, but not in others, causing a strong increase in the integrated MLR of the former. Therefore, we do not claim that the integrated MLRs quoted here are representative of any particular galaxy trait.

4.3.1. *Uncertainties in the Mass-Loss Rates*

As emphasized in papers I & II, there are major uncertainties in deriving MLRs for AGB stars using only 3.6 and 4.5 μm photometry. The first is a degeneracy between τ and T_{eff} : cool stars with small MLRs can have the same [3.6] – [4.5] color as warmer stars with strong MLRs. This uncertainty most strongly affects the bluest AGB candidates([3.6] – [4.5] < 0.5), but is of little consequence for the redder AGB candidates, where the MLR is much less sensitive to T_{eff} . This uncertainty may also be exacerbated by atmospheric molecular absorption, which can affect IRAC colors, although these effects have not yet been quantified (Marengo et al. 2007). Since the reddest AGB stars also have the strongest MLRs, the integrated MLR for each galaxy and the individual MLRs for the red stars is robust.

The second major uncertainty lies with the choice of the chemical composition of the AGB winds. With no information about the wind compositions, we must make the unlikely assumption of a single composition for the entire AGB population. The integrated MLRs computed for different wind compositions vary by up to a factor of eight.

While these uncertainties affect the MLRs of individual sources, the integrated MLR is heavily affected by the unfortunate placement of background galaxies in the same region of the CMD as the mass-losing AGB stars, as discussed above. While we have attempted to remove this contamination, we must still emphasize that the integrated MLRs reported here are meant as first-order estimates only.

4.3.2. *ISM Gas Return*

While massive stars occasionally provide bursts of feedback to the ISM when they explode as supernovae, it is the more numerous, mass-losing stars that dominate long-term gas return. Gas return from massive stars occurs only during and shortly after a burst of star formation, whereas AGB gas return is continuous over time and allows galaxies to gradually rebuild an ISM while remaining in quiescence with regard to star formation. A comparison between the returned mass and the mass used to form stars ($f_{\text{return}} = \dot{M}_{\text{dusty}}/\text{SFR}_{(1\text{Gyr})}$), computed using current integrated MLRs (bottom panel of Table 8) and the average SFRs over the last 1 Gyr (Orban et al. 2008), shows that each galaxy in our sample has been undergoing a SFR that is unsustainable, with the exception of LGS 3 and DDO 210. Without another source of gas to the ISM or a change in star formation rate, these galaxies will exhaust their supply of interstellar gas (see Table 9). We note that there are uncertainties associated with converting SFHs derived from partial fields to global SFHs, but we believe that these SFHs should be qualitatively representative

of the galaxies.

It is unlikely that these galaxies can accrete significant amounts of gas from their surrounding environments, as they are all isolated from other systems. If these galaxies are to maintain their current SFRs, there must be some non-dusty mass loss in addition to the dust-traced mass loss measured here. If the ISM is replenished solely by stellar mass loss (dusty plus non-dusty), then f_{return} (Table 9) reflects what fraction of the total stellar mass loss is traced by dust. We find that in Sextans A, WLM, and IC 1613, dusty mass loss accounts for only 2% – 4% of the total mass loss required to replenish the ISM at a rate equal to the current SFR, while in Phoenix, Leo A, and Pegasus dIrr, this fraction rises to 22% – 30%. Previous work by McDonald & van Loon (2007) and McDonald et al. (2009) found that roughly 50% of the mass loss is traced by dust in globular clusters. The very large amount of non-dusty mass loss required to balance the SFRs in Sextans A, WLM, and IC 1613 suggests that the current SFRs in these galaxies are indeed unsustainable.

The AGB stars in LGS 3 and DDO 210 are losing mass at a rate faster than new stars are currently being formed. Therefore, barring any outside influences, the mass loss traced by dust in these galaxies is sufficient to replenish the ISM at a rate that can sustain the ISM recycling rate indefinitely, eliminating the need for other gas return mechanisms such as non-dusty mass loss and gas accretion.

By comparing the H I mass in each galaxy with the current SFR and dusty MLR, we can compute the life expectancy of each galaxy, or the timescale before the galaxy runs out of H I gas. This timescale is known as the “Roberts time” (Sandage 1986), corrected so that it now includes gas return:

$$\tau_{\text{R,corrected}} = \left(1 - \frac{\dot{M}_{\text{dusty}}}{\text{SFR}} \right)^{-1} \frac{M_{\text{gas}}}{\text{SFR}}. \quad (1)$$

The correction factor is referred to as the recycling factor. We find that Leo A and Phoenix can survive as gas-rich dwarf galaxies for 17 Gyr and 76 Gyr, respectively, but that Pegasus dIrr, Sextans A, WLM, and IC 1613 can continue star formation activity at the current rate for only 2.5 Gyr – 6.8 Gyr, with WLM being the first galaxy to become inactive (Table 9). For Leo A, Phoenix, and Pegasus dIrr, dusty mass loss is responsible for an increase of 29% – 40% over the uncorrected τ_{R} , while in the remaining three galaxies, dusty mass loss is responsible for a mere 2% – 4% increase. For disk galaxies, Kennicutt et al. (1994) finds that this increase can be significantly larger, although we note that those estimates include mass lost during all stages of stellar evolution.

Assuming a closed-box model, and that the average SFR over the last 5 Gyr represents the average rate over each galaxies’ lifetime, then when including gas return from dusty stellar mass loss, we find that the predicted gas-rich lifetimes of WLM and IC 1613 ($\tau_{\text{lifetime}} = 3.7$ and 4.3 Gyr, respectively, see Table 9) are shorter than the current estimate of the mean mass-weighted stellar ages for each galaxy ($\tau_{\text{age}} = 6.7$ and 7.7 Gyr, respectively; Orban et al. 2008). Even if we assume that dusty mass loss accounts for only 10% of the total mass loss, we still find lifetimes that are too short to allow for any current star formation in WLM and IC 1613 ($\tau_{\text{lifetime}} = 5.8$ and 5.7 Gyr, respectively). This indicates that either these galaxies have been accreting gas from the outside or

that they have been very inefficient at using up their initial gas to form stars, although it is unclear what might cause the latter (Orban et al. 2008).

5. SUMMARY OF RESULTS AND CONCLUSIONS

We present part III of a *Spitzer* IRAC census of AGB stars in eight Local Group dwarf irregular galaxies: Phoenix, LGS 3, DDO 210, Leo A, Pegasus dIrr, Sextans A, WLM, and IC 1613. Stars brighter than the $3.6 \mu\text{m}$ TRGB are identified as AGB candidates, and we find that 50% – 100% of these sources are detected and identified as AGB stars in broadband optical photometry. An optical completeness fraction of 70% agrees within the errors of all eight galaxies in our sample, suggesting that optical surveys of dwarf galaxies are underrepresenting the AGB by 30% – 40%, due to extinction from circumstellar dust.

We find no trend of decreasing optical completeness with increasing metallicity, as would be expected assuming that dust is more efficiently produced at high metallicities. This suggests that dust production is not suppressed at low metallicity, although it may form in smaller quantities. We do however see that the fraction of moderately red (dusty) stars that are not obscured in the optical increases in galaxies with higher metallicity.

Known carbon stars were identified in our IRAC data, and we find that previous studies have used only a small fraction (26% – 34%) of the population of M and C stars to compute C/M ratios.

Using the [3.6]–[4.5] color excess, we compute average individual stellar mass-loss rates ranging from $3.1 \times 10^{-7} - 6.6 \times 10^{-6} M_{\odot} \text{ yr}^{-1}$, agreeing well with estimates of AGB MLRs in other studies. Mass loss traced by dust does not appear to be inhibited at low metallicity.

The integrated MLRs for each galaxy range from $4.4 \times 10^{-5} - 1.4 \times 10^{-3} M_{\odot} \text{ yr}^{-1}$. Normalized to the total stellar mass, we find a range of $\dot{M}_{\text{Tot}}/M_{*} = 2 \times 10^{-8}$ for LGS 3, to $\dot{M}_{\text{Tot}}/M_{*} = 6 \times 10^{-10}$ for Leo A. These rates do not include mass loss that is unaccompanied by dust.

A comparison of the recent (within 1 Gyr) SFR and the current MLRs reveals that all but two of our galaxies (LGS 3 and DDO 210) cannot sustain their current SFR solely through ISM gas return from the stellar mass-loss rates measured here. Phoenix, Leo A, Pegasus dIrr, Sextans A, WLM, and IC 1613 will all eventually extinguish their gas supply unless there is an additional supply of gas. In these galaxies, mass loss traced by dust can account for only 2% – 30% of the material required to maintain the current SFR.

We thank Alan McConnachie and Vidas Vansevicius for sharing the Subaru photometry of DDO 210 and Leo A, respectively, and Sebastian Hidalgo and the LCID team for providing ACS data of LGS 3. We also thank Dale Jackson for many helpful discussions. Support for this work was provided by NASA through contract 1314733, 1256406, and 1215746 issued by JPL, Caltech to the University of Minnesota. MLB recognizes support from the University of Minnesota Louise T. Dossdall and Dissertation Fellowships.

REFERENCES

- Abell, G. O. 1995, *VizieR Online Data Catalog*, 7004, 0
- Albert, L., Demers, S., & Kunkel, W. E. 2000, *AJ*, 119, 2780
- Asplund, M., Grevesse, N., Sauval, A. J., Allende Prieto, C., & Kiselman, D. 2004, *A&A*, 417, 751
- Barnes, D. G., & de Blok, W. J. G. 2004, *MNRAS*, 351, 333
- Battinelli, P., & Demers, S. 2000, *AJ*, 120, 1801
- Battinelli, P., & Demers, S. 2004, *A&A*, 416, 111
- Battinelli, P., & Demers, S. 2005, *A&A*, 434, 657
- Blum, R. D., et al. 2006, *AJ*, 132, 2034
- Bolatto, A. D., et al. 2007, *ApJ*, 655, 212
- Boyer, M. L., McDonald, I., van Loon, J. Th., Woodward, C. E., Gehrz, R. D., Evans, A., Dupree, A. K. 2008, *AJ*, 135, 1395
- Boyer, M. L., Woodward, C. E., van Loon, J. Th., Gordon, K. D., Evans, A., Gehrz, R. D., Helton, L. A., & Polomski, E. F. 2006, *AJ*, 132, 1415
- Cannon, J. M., Skillman, E. D., Garnett, D. R., & Dufour, R. J. 2002, *ApJ*, 565, 931
- Cioni, M.-R. L., et al. 2003, *A&A*, 406, 51
- Cole, A. A., et al. 2007, *ApJ*, 659, L17
- Da Costa, G. S. 1994, *Dwarf Galaxies*, 221
- Dohm-Palmer, R. C., et al. 1997, *AJ*, 114, 2527
- Dohm-Palmer, R. C., Skillman, E. D., Mateo, M., Saha, A., Dolphin, A., Tolstoy, E., Gallagher, J. S., & Cole, A. A. 2002, *AJ*, 123, 813
- Dolphin, A. E., et al. 2001, *ApJ*, 550, 554
- Dolphin, A. E., et al. 2002, *AJ*, 123, 3154
- Dolphin, A. E., et al. 2003a, *AJ*, 125, 1261
- Dolphin, A. E., et al. 2003b, *AJ*, 126, 187
- Dolphin, A. E., Weisz, D. R., Skillman, E. D., & Holtzman, J. A. 2005, *ArXiv Astrophysics e-prints*, arXiv:astro-ph/0506430
- Fazio, G. G., et al. 2004, *ApJS*, 154, 10
- Fernandez, A., Mathez, G., & Nottale, L. 1996, *VizieR Online Data Catalog*, 7088, 0

- Gail, H.-P., & Sedlmayr, E. 1986, *A&A*, 161, 201
- Gallagher, J. S., Tolstoy, E., Dohm-Palmer, R. .C., Skillman, E. D., Cole, A. A., Hoessel, J. G., Saha, A., & Mateo, M. 1998, *AJ*, 115, 1869
- Gallart, C. 2008, *Astronomical Society of the Pacific Conference Series*, 390, 278
- Gehrz, R. 1989, *Interstellar Dust*, 135, 445
- Gehrz, R. D., et al. 2007, *Review of Scientific Instruments*, 78, 011302
- Gehrz, R. D., & Woolf, N. J. 1971, *ApJ*, 165, 285
- Giovanelli, R., & Haynes, M. P. 1993, *AJ*, 105, 1271
- Girardi, L., & Marigo, P. 2007, *A&A*, 462, 237
- Groenewegen, M. A. T. 2006, *A&A*, 448, 181
- Gruendl, R. A., Chu, Y. -, Seale, J. P., Matsuura, M., Speck, A. K., Sloan, G. C., & Looney, L. W. 2008, *arXiv:0809.5107*
- Gullieuszik, M., Rejkuba, M., Cioni, M. R., Habing, H. J., & Held, E. V. 2007, *A&A*, 475, 467
- Hoffman, G. L., Salpeter, E. E., Farhat, B., Roos, T., Williams, H., & Helou, G. 1996, *ApJS*, 105, 269
- Holtzman, J. A., Afonso, C., & Dolphin, A. 2006, *ApJS*, 166, 534
- Holtzman, J. A., Smith, G. H., & Grillmair, C. 2000, *AJ*, 120, 3060
- Huchtmeier, W. K., Seiradakis, J. H., & Materne, J. 1981, *A&A*, 102, 134
- Indebetouw, R., et al. 2005, *ApJ*, 619, 931
- Jackson, D. C., Cannon, J. M., Skillman, E. D., Lee, H., Gehrz, R. D., Woodward, C. E., Polomski, E. 2006, *ApJ*, 646, 192
- Jackson, D. C., Skillman, E. D., Gehrz, R. D., Polomski, E., Woodward, C. E. 2007a, *ApJ*, 656, 818
- Jackson, D. C., Skillman, E. D., Gehrz, R. D., Polomski, E., Woodward, C. E. 2007b, *ApJ*, 667, 891
- Jura, M. 1984, *ApJ*, 282, 200
- Kennicutt, R., et al. 2007, *Bulletin of the American Astronomical Society*, 38, 894
- Kennicutt, R. C., Jr., Tamblyn, P., & Congdon, C. E. 1994, *ApJ*, 435, 22
- Lagadec, E., & Zijlstra, A. A. 2008, *MNRAS*, 390, L59

- Lee, H., Skillman, E. D., Cannon, J. M., Jackson, D. C., Gehrz, R. D., Polomski, E. F., & Woodward, C. E. 2006, *ApJ*, 647, 970
- Lee, M. G. 1995, *AJ*, 110, 1129
- Lee, M. G., Aparicio, A., Tikonov, N., Byun, Y.-I., & Kim, E. 1999, *AJ*, 118, 853
- Lo, K. Y., Sargent, W. L. W., & Young, K. 1993, *AJ*, 106, 507
- Loup, C., Zijlstra, A. A., Waters, L. B. F. M., & Groenewegen, M. A. T. 1997, *A&AS*, 125, 419
- Makovoz, D., & Marleau, F. R. 2005, *PASP*, 117, 1113
- Marengo, M., Hora, J. L., Barmby, P., Willner, S. P., Allen, L. E., Schuster, M. T., & Fazio, G. G. 2007, *Why Galaxies Care About AGB Stars: Their Importance as Actors and Probes*, 378, 80
- Marigo, P., Girardi, L., Bressan, A., Groenewegen, M. A. T., Silva, L., & Granato, G. L. 2008, *A&A*, 482, 883
- Massey, P., Olsen, K. A. G., Hodge, P. W., Strong, S. B., Jacoby, G. H., Schlingman, W., & Smith, R. C. 2006, *AJ*, 131, 2478
- Mateo, M. L. 1998, *ARA&A*, 36, 435
- McConnachie, A. W., Arimoto, N., Irwin, M., & Tolstoy, E. 2006, *MNRAS*, 373, 715
- McDonald, I., & van Loon, J. T. 2007, *A&A*, 476, 1261
- McDonald, I., van Loon, J. Th., Decin, L., Boyer, M. L., Woodward, C. E., Gehrz, R. D., Evans, A., & Dupree, A. K. 2008, *MNRAS*, in press
- Menzies, J., Feast, M., Whitelock, P., Olivier, E., Matsunaga, N., & Da Costa, G. 2008, *MNRAS*, 385, 1045
- Miller, B. W., Dolphin, A. E., Lee, M. G., Kim, S. C., & Hodge, P. 2001, *ApJ*, 562, 713
- Orban, C., Gnedin, O. Y., Weisz, D. R., Skillman, E. D., Dolphin, A. E., & Holtzman, J. A. 2008, *ApJ*, 686, 1030
- Reach, W. T., et al. 2005, *PASP*, 117, 978
- Rieke, G. H., & Lebofsky, M. J. 1985, *ApJ*, 288, 618
- Robin, A. C., Reyl , C., Derri re, S., & Picaud, S. 2003, *A&A*, 409, 523
- Sandage, A. 1986, *A&A*, 161, 89
- Sanders, D. B., et al. 2007, *ApJS*, 172, 86
- Sloan, G. C., Kraemer, K. E., Wood, P. R., Zijlstra, A. A., Bernard-Salas, J., Devost, D., & Houck, J. R. 2008, *arXiv:0807.2998*

- Spitzer* Science Center. 2006, Infrared Array Camera Data Handbook (Pasadena: SSC), <http://ssc.spitzer.caltech.edu/irac/dh/>
- Stetson, P. B. 1987, *PASP*, 99, 191
- Trams, N. R., et al. 1999, *A&A*, 346, 843
- van Loon, J. Th. 2006, in ASP Conf. Ser. 353, *Stellar Evolution at Low Metallicity: Mass Loss, Explosions, Cosmology*, ed. H. Lamers et al. (San Francisco: ASP), 211
- van Loon, J. Th., Cohen, M., Oliveira, J. M., Matsuura, M., McDonald, I., Sloan, G. C., Wood, P. R., & Zijlstra, A. A. 2008, *A&A*, 487, 1055
- van Loon, J. Th., Groenewegen, M. A. T., de Koter, A., Trams, N. R., Waters, L. B. F. M., Zijlstra, A. A., Whitelock, P. A., & Loup, C. 1999, *A&A*, 351, 559
- van Loon, J. Th., Marshall, J. R., & Zijlstra, A. A. 2005, *A&A*, 442, 597
- van Loon, J. Th., McDonald, I., Oliveira, J. M., Evans, A., Boyer, M. L., Gehrz, R. D., Polomski, E., & Woodward, C. E. 2006, *A&A*, 450, 339
- Vansevičius, V., et al. 2004, *ApJ*, 611, L93
- van Zee, L., Skillman, E. D., Haynes, M. P. 2006, *ApJ*, 637, 269
- Vassiliadis, E., & Wood, P. R. 1993, *ApJ*, 413, 641
- Volders, L. M. J. S., & Högbom, J. A. 1961, *Bull. Astron. Inst. Netherlands*, 15, 307
- Werner, M. W., et al. 2004, *ApJS*, 154, 1
- Whitelock, P. A., Feast, M. W., van Loon, J. T., & Zijlstra, A. A. 2003, *MNRAS*, 342, 86
- Whitelock, P. A., Menzies, J., Feast, M., Matsunaga, N., Tanabé, T., Ita, Y. 2008, arXiv:0812.0903
- Whitney, B. A., et al. 2008, *AJ*, 136, 18
- Young, L. M., & Lo, K. Y. 1996, *ApJ*, 462, 203
- Young, L. M., Skillman, E. D., Weisz, D. R., & Dolphin, A. E. 2007, *ApJ*, 659, 331

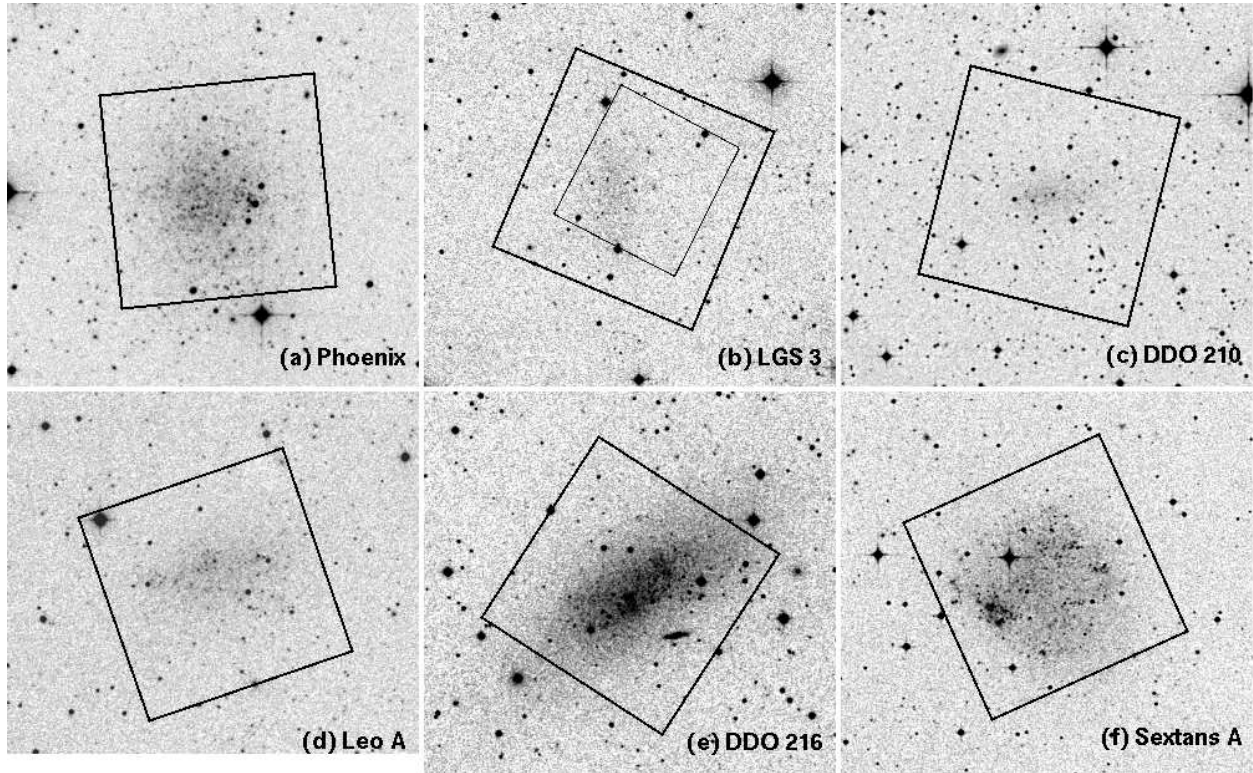


Fig. 1.— Digitized Sky Survey (DSS) images of (a) Phoenix, (b) LGS 3, (c) DDO 210, (d) Leo A, (e) Pegasus dIrr, and (f) Sextans A. The field shown in each panel is $9.7' \times 9.5'$. The IRAC field of view is overplotted with a thick line. The optical coverage for each galaxy, with the exception of LGS 3, is larger than the DSS image shown. (b) shows the HST ACS field of view for LGS 3 plotted as a thin black line. In all six galaxies, the IRAC coverage contains the vast majority of the stellar population.

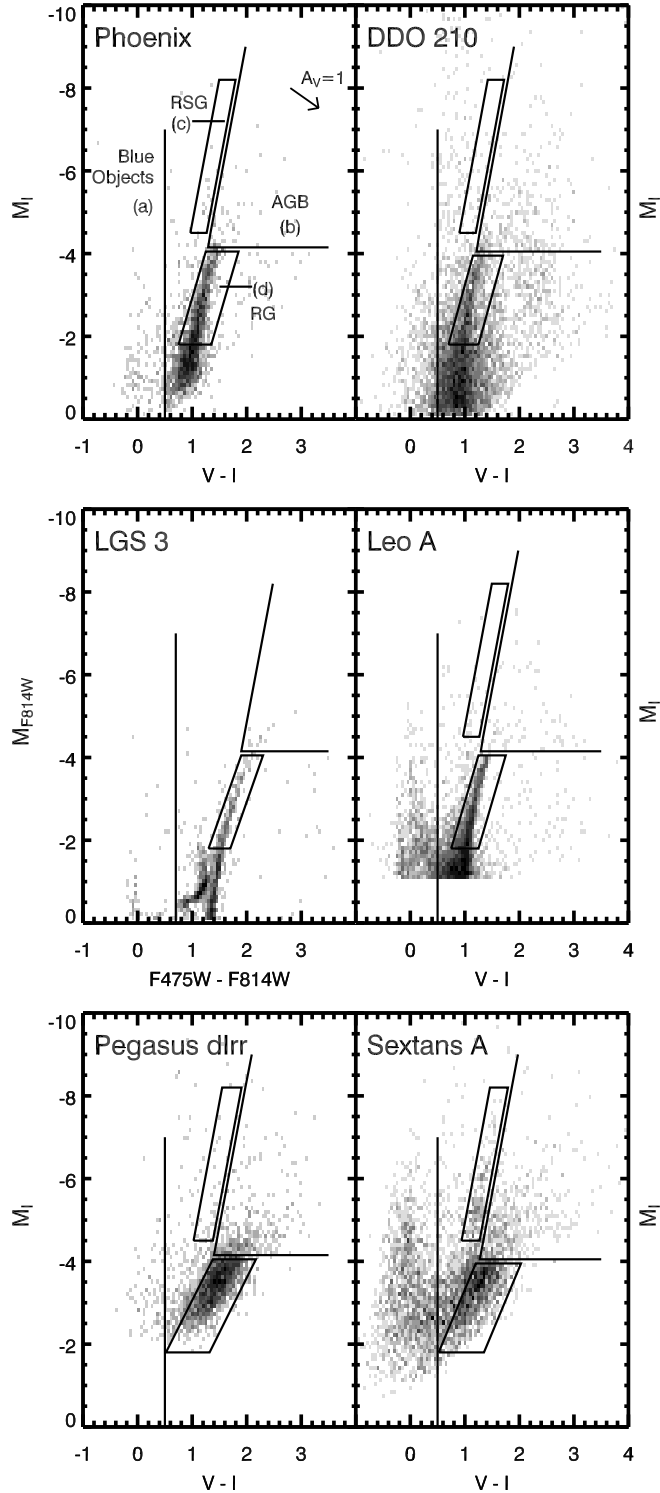


Fig. 2.— Optical color-magnitude diagrams. See § 2.3 for a description of optical photometry. The color magnitude diagrams are represented by Hess diagrams with color bins and magnitude bins of 0.5 mag. Regions are labeled containing (a) blue objects, (b) AGB stars, (c) RSGs, and (d) red giant stars. These optical identifications are used to aid in the identification of different source types in the infrared color-magnitude diagrams. The I -band TRGB is approximately $M_I = -4.0$ mag for each galaxy. The space between the gaps represent the approximate 1σ photometric uncertainties. A vector in the first panel shows 1 magnitude of extinction and the associated reddening.

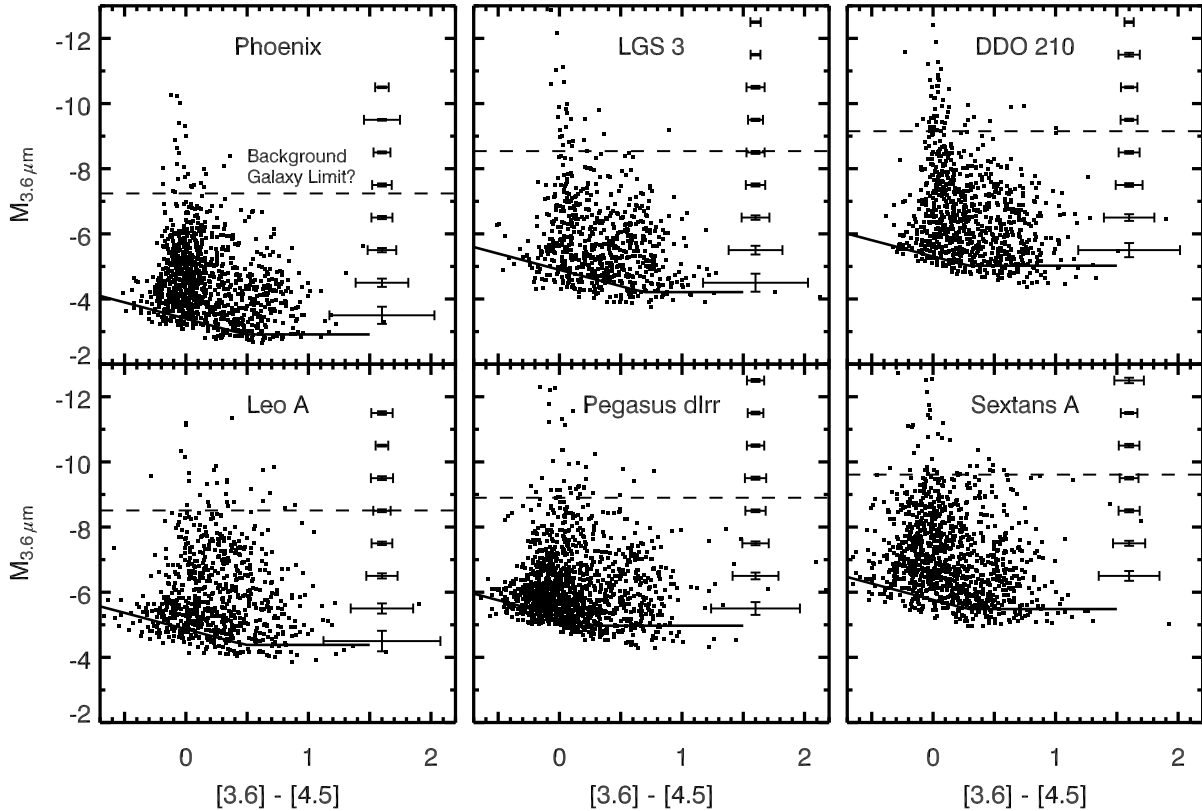


Fig. 3.— $[3.6]$ vs. $[3.6] - [4.5]$ color-magnitude diagrams. All point sources detected at 3.6 and 4.5 μm are included. 1σ photometric errors averaged over 1 mag bins are shown on the right of each panel. The solid lines represent the 50% completeness limits. The dashed line shows the position of $m_{3.6} = 16$ mag, which is the approximate maximum apparent magnitude of point-source background galaxies. Red sources above this line are very likely obscured AGB stars, since background galaxies brighter than this limit are likely extended and subsequently rejected during PSF fitting.

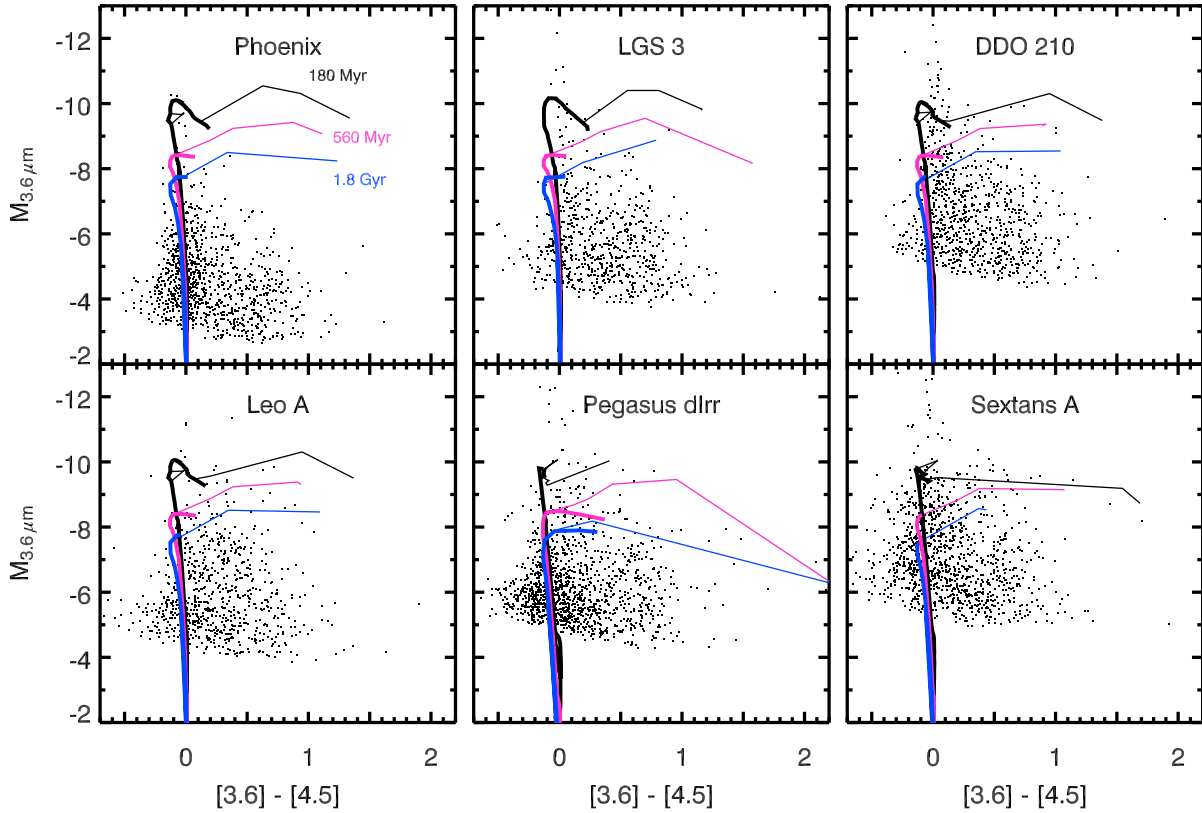


Fig. 4.— Color-magnitude diagrams, as in Figure 3, with overlaid isochrones from Marigo et al. (2008). Isochrones were computed at the metallicity of each galaxy for three separate single-age populations: $\log(t) = 8.25$ (black), 8.75 (magenta), and 9.25 (blue). The thick lines represent isochrones for stars with no circumstellar dust, and the thin lines are isochrones for stars with dust. Dust compositions are assumed to be 60% silicates plus 40% aluminum oxides for O-rich stars and 85% amorphous carbon plus 15% SiC for C-rich stars. Mass-losing AGB stars are expected to be among the brightest and reddest stars in the CMDs.

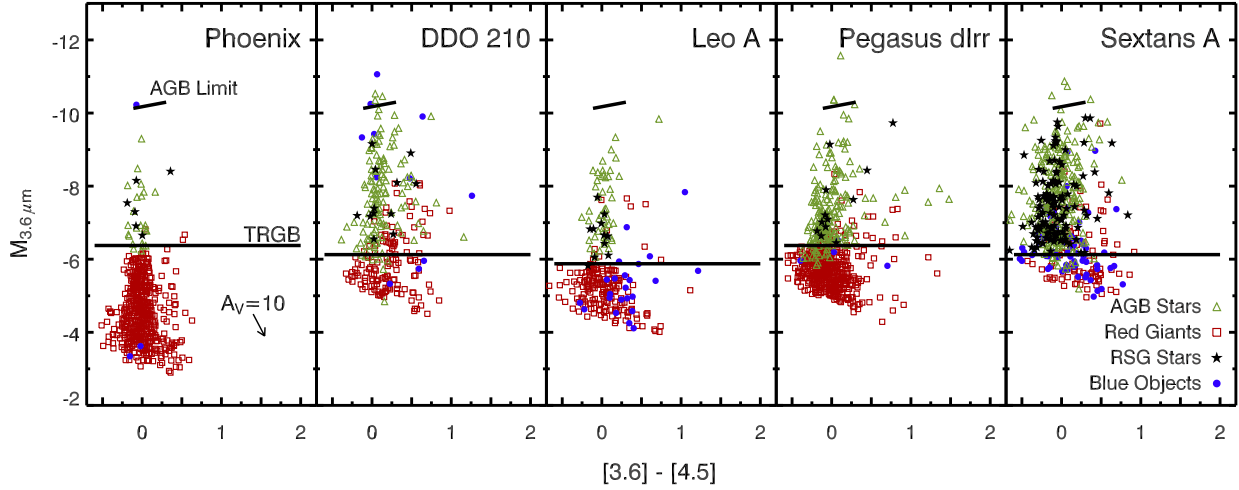


Fig. 5.— Optically identified sources in the $[3.6]$ vs. $[3.6] - [4.5]$ color-magnitude diagrams. Red squares are red giants, black stars are RSGs, blue circles are blue objects, and green triangles are optical AGB stars, as identified in Figure 2. The first panel displays a vector showing 10 visual magnitudes of extinction and the associated reddening. Note that there is virtually no extinction at $3.6 \mu\text{m}$. Each panel shows the AGB limit and the location of the TRGB. Note that red stars above the TRGB, evident in Figures 3 and 4, are largely undetected in the optical.

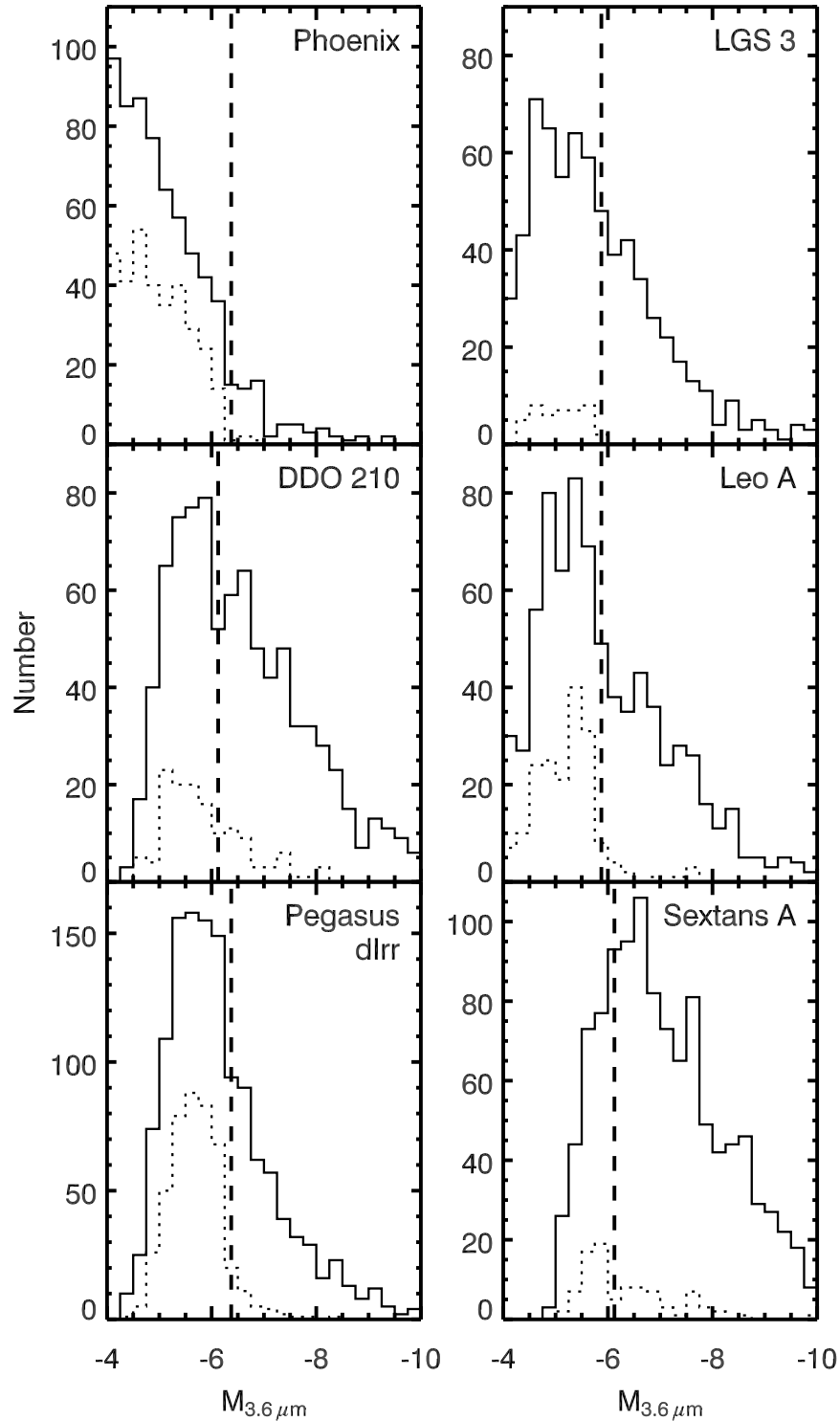


Fig. 6.— 3.6 μm luminosity functions. The solid line represents all sources detected at 3.6 and 4.5 μm . The dotted line shows optically classified sub-TRGB stars. The adopted TRGB values are marked with a dashed line. In the case of Sextans A, where the IRAC luminosity function drops off at a magnitude brighter than the TRGB, the optical sub-TRGB luminosity function provides a first-order estimate of the 3.6 μm TRGB.

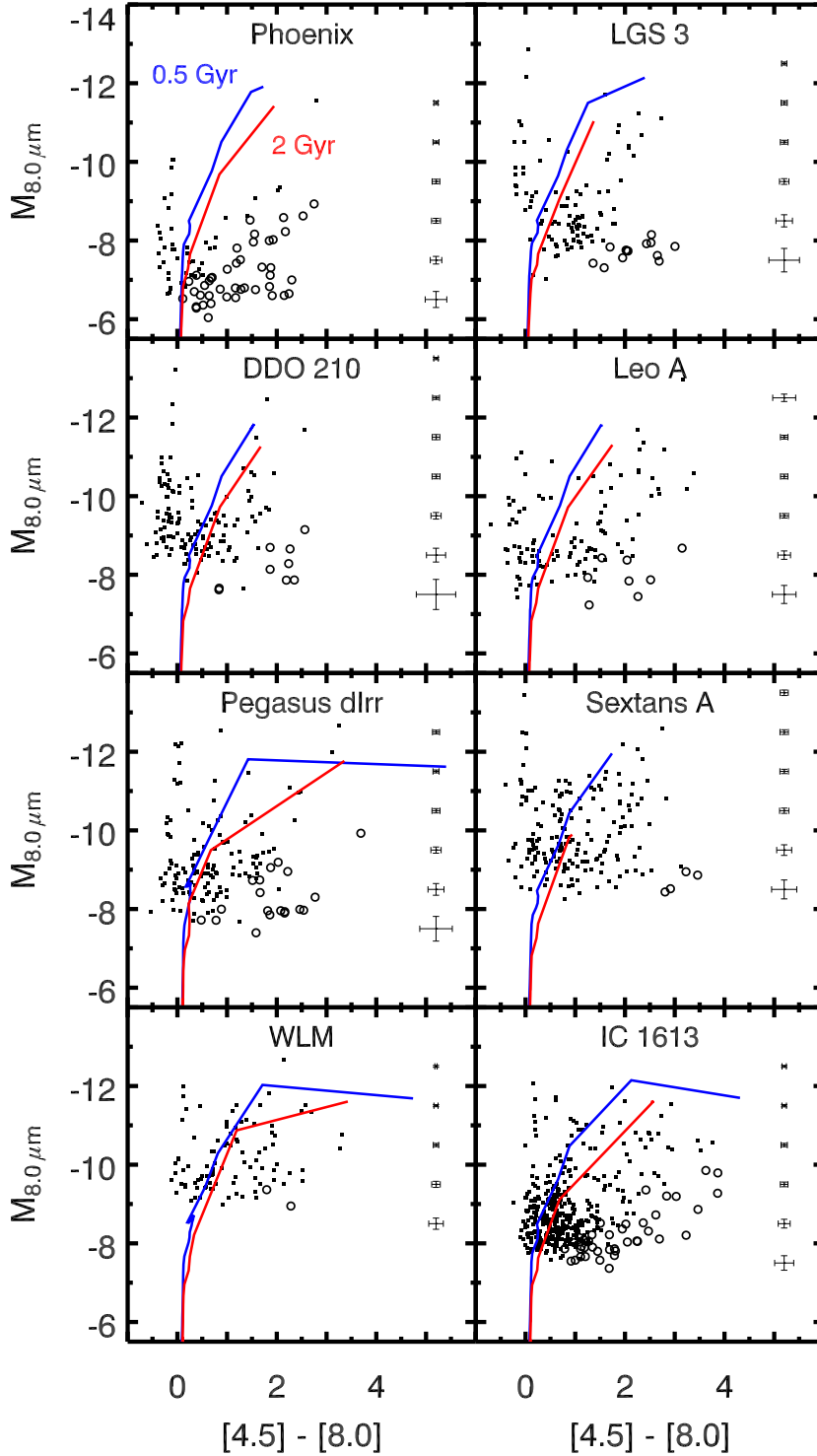


Fig. 7.— $[8.0]$ vs. $[4.5] - [8.0]$ color-magnitude diagrams. Photometric 1σ errors, averaged over 1 magnitude bins, are shown on the right side of each panel. Open circles mark sources that are below the $3.6\ \mu\text{m}$ TRGB. In each galaxy, a plume of bright, red stars generally falls just redward of the isochrones for mass-losing AGB stars (Marigo et al. 2008). The isochrones were computed using the metallicities listed in Table 1, and a single-age population of 2 Gyr (red line) and 0.5 Gyr (blue line). Assumed dust compositions are identical to those in Figure 4.

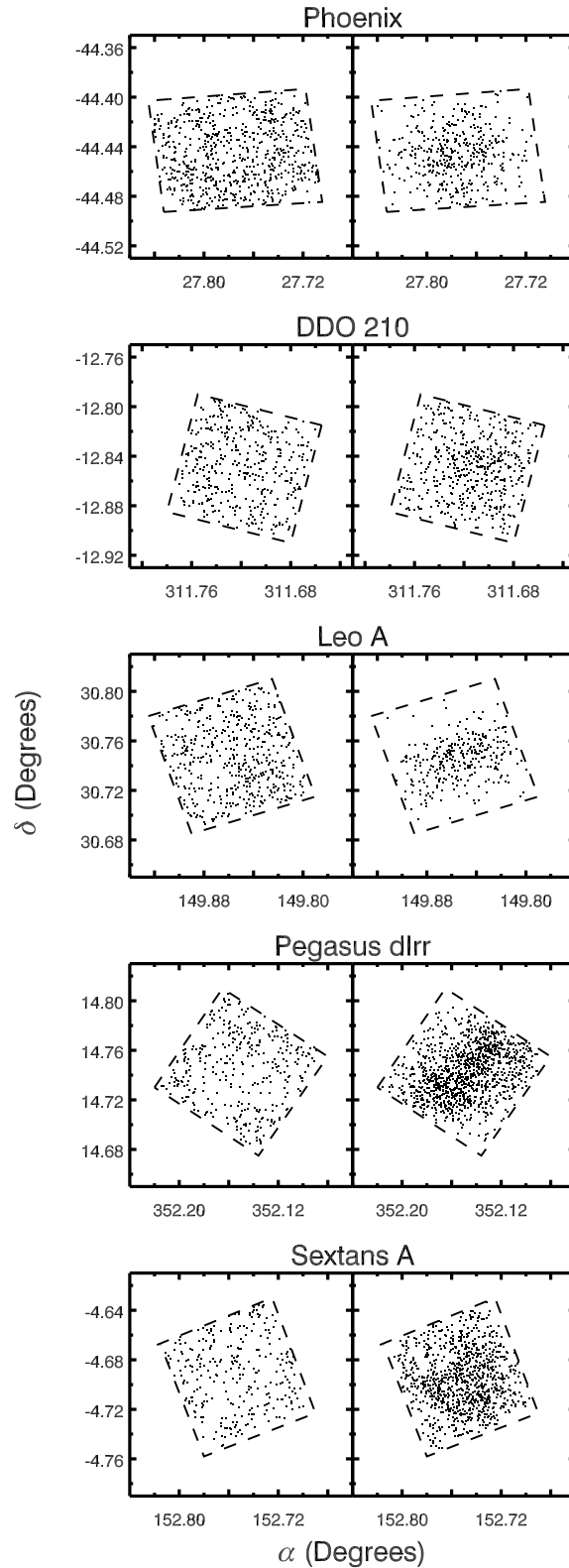


Fig. 8.— Spatial distributions of *all* IR sources without (*left*) and with (*right*) optical counterparts, where a source is considered undetected in the optical if $M_I > -2.5$ mag. Sources without optical counterparts are likely either dust-enshrouded AGB stars or background galaxies (and possibly YSOs). The sources in the left panels do not cluster towards the centers of the galaxies, suggesting at least some of them are not truly AGB stars.

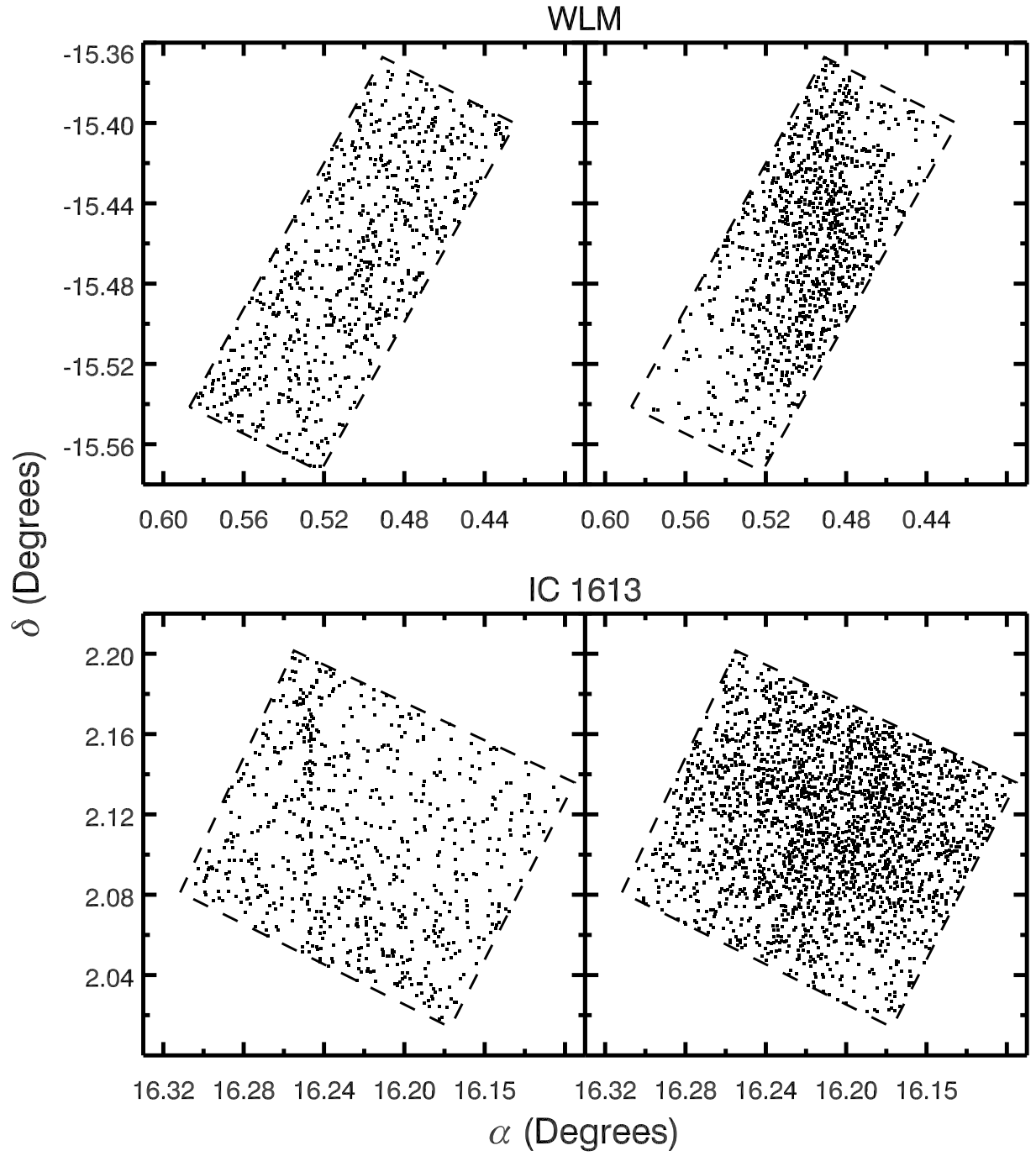


Fig. 9.— Same as Figure 8 for WLM and IC 1613.

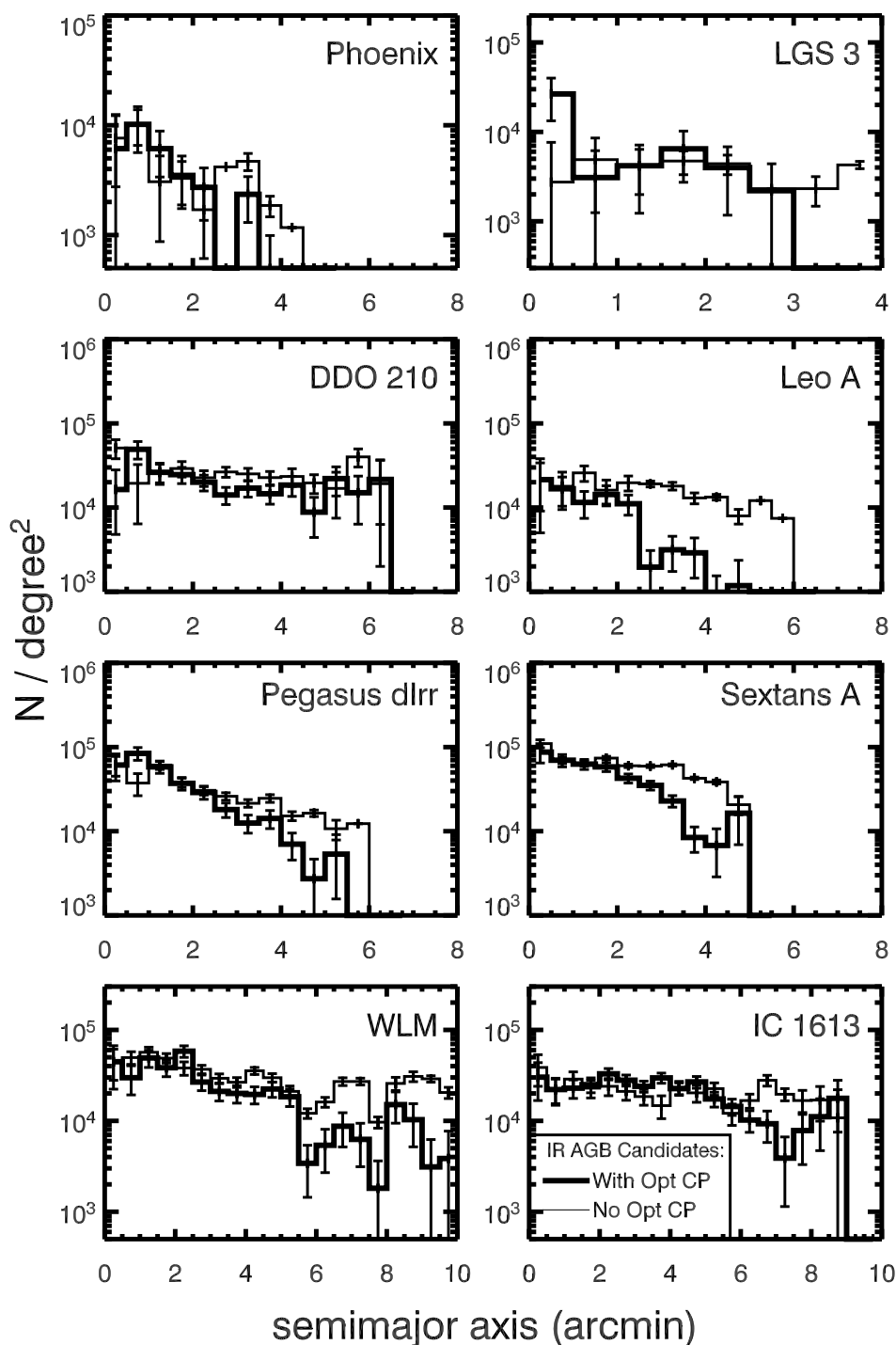


Fig. 10.— Radial density profiles for IR AGB candidates with optical counterparts (“Opt CPs”) brighter than (thick line) and fainter than (thin line) the I -band TRGB, with the latter normalized to the former. Profiles were determined using ellipsoidal annuli with semi-major axis bins of $0.5'$ centered on each galaxy. If these two populations are obscured and non-obscured AGB stars, the two profiles should be identical. However, it is clear that a flat distribution of background galaxies is contaminating most of our targets. We have fit the declining profile plus a flat distribution to each profile for sources without optical counterparts to measure the background contamination, but the uncertainties in the fits are large and would be much improved by observing larger fields of view.

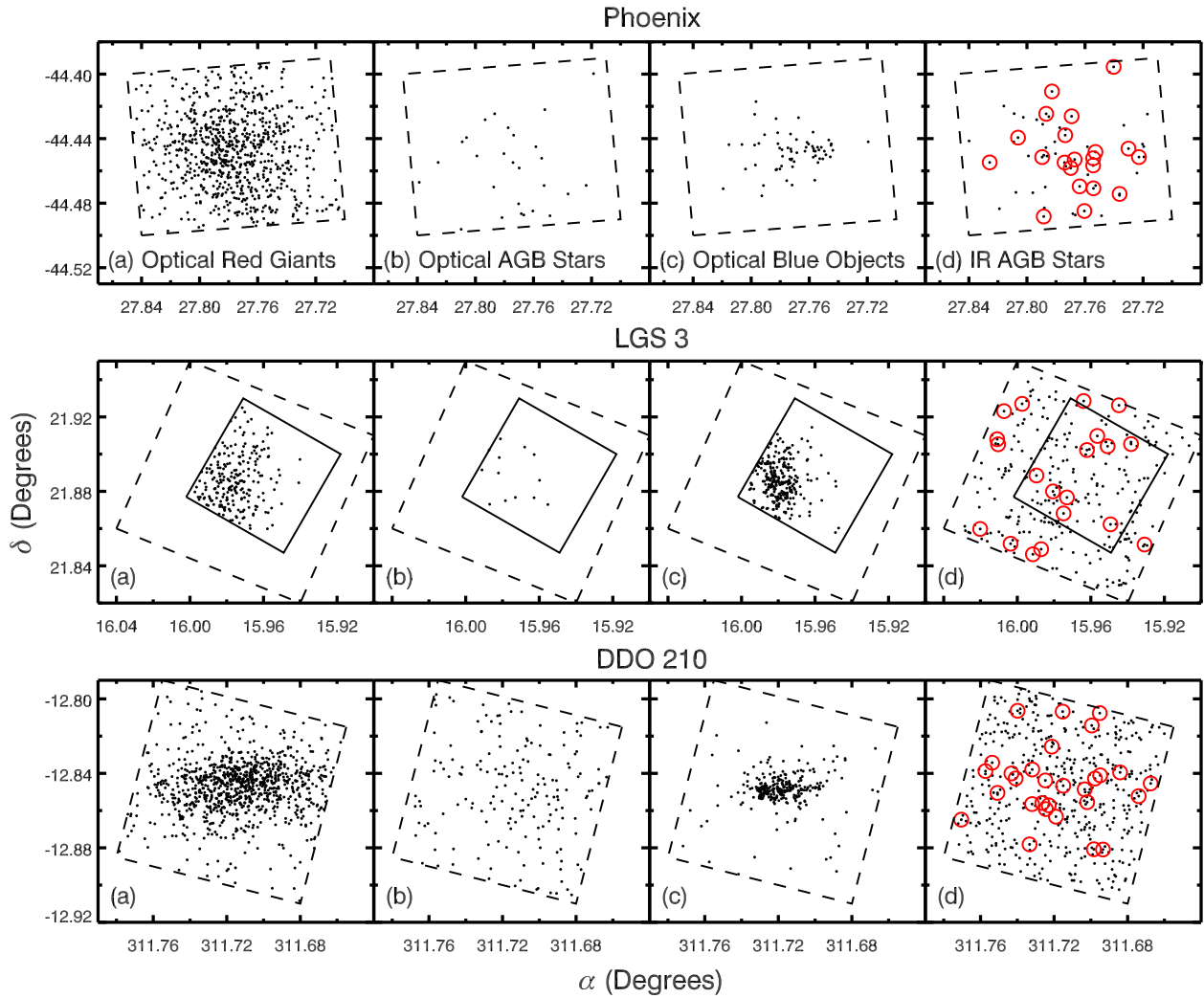


Fig. 11.— Stellar spatial distributions of (a) optical red giants, (b) optical AGB stars, (c) optical blue objects, and (d) IR-identified AGB candidates in Phoenix, LGS 3, and DDO 210. The dashed lines outline the *Spitzer* coverage. The solid box in each LGS 3 panel shows the area covered by optical data. In each panel (d), AGB candidates brighter than $m_{3.6} = 16$ mag are plotted with open red circles in order to show the distribution of AGB stars with little to no contamination from background galaxies.

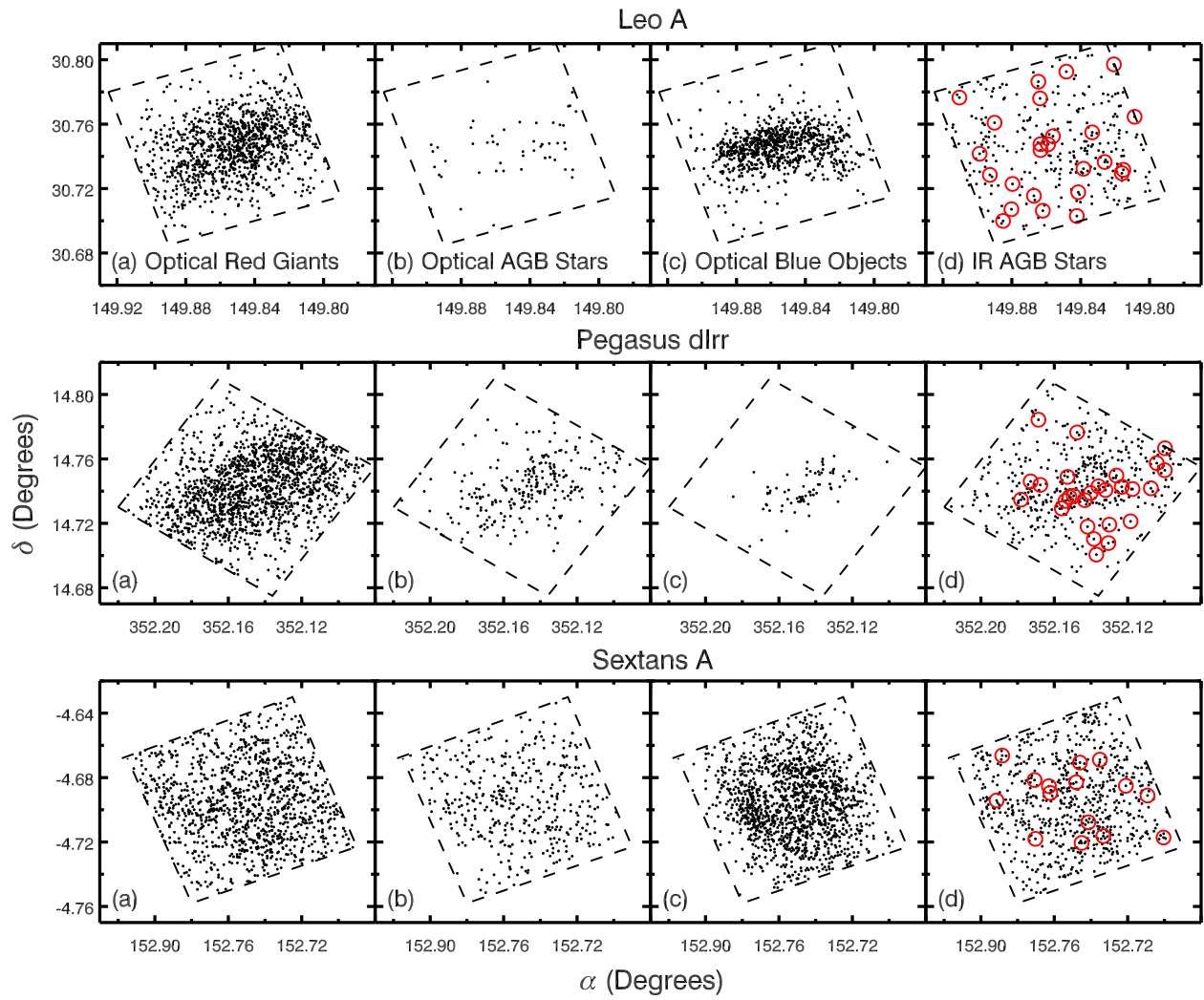


Fig. 12.— Stellar spatial distributions for Leo A, Pegasus dIrr, and Sextans A. The panels are the same as in Figure 11.

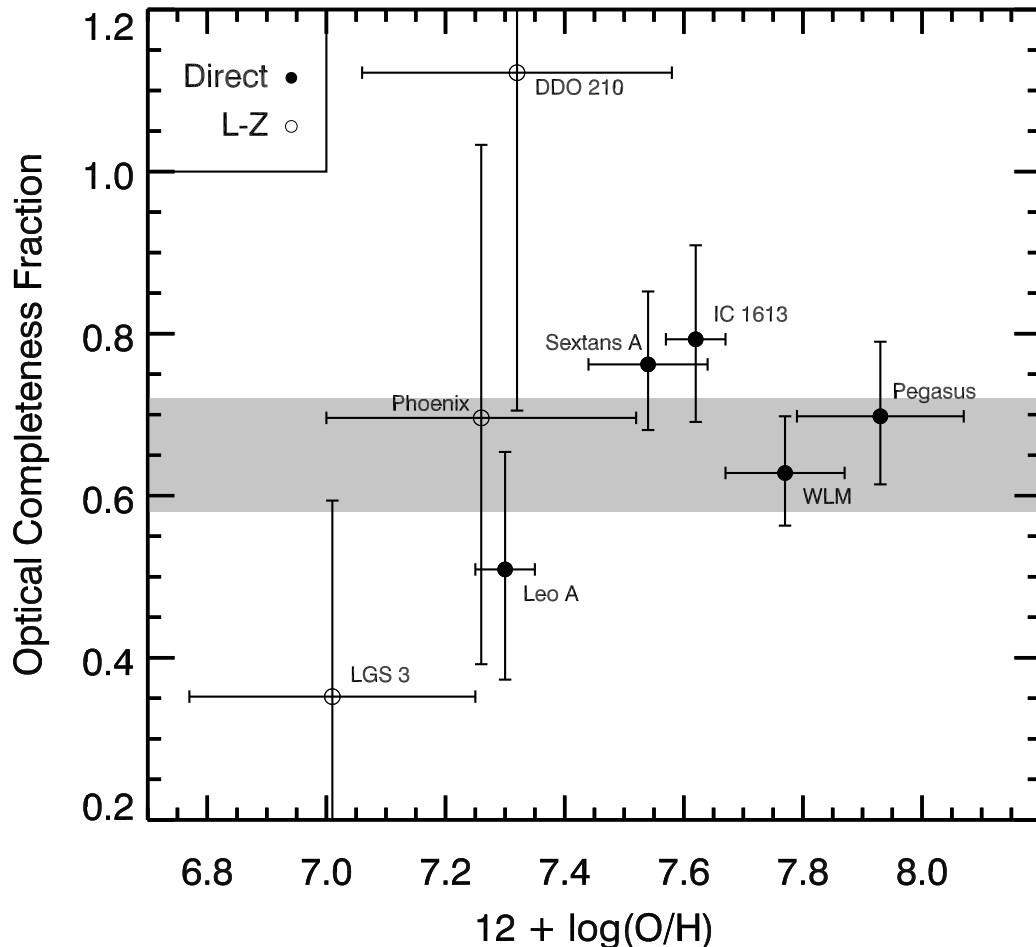


Fig. 13.— Optical completeness fraction vs. metallicity. Closed circles are galaxies with metallicities from van Zee et al. (2006), and open circles show galaxies whose metallicities were determined using the L - Z relationship from Lee et al. (2006). The optical completeness fraction is computed by first estimating the true background galaxy contamination by fitting a flat contribution to the radial density profile of IR AGB candidates (Fig. 10). The errors include the 1σ uncertainties in the fit, Poisson statistics, and foreground star contamination. We find no convincing correlation between optical completeness and metallicity, indicating that dust production is not inhibited at low metallicity. An optical completeness fraction of approximately 60% to 70% is consistent with the data for all eight galaxies (shaded region).

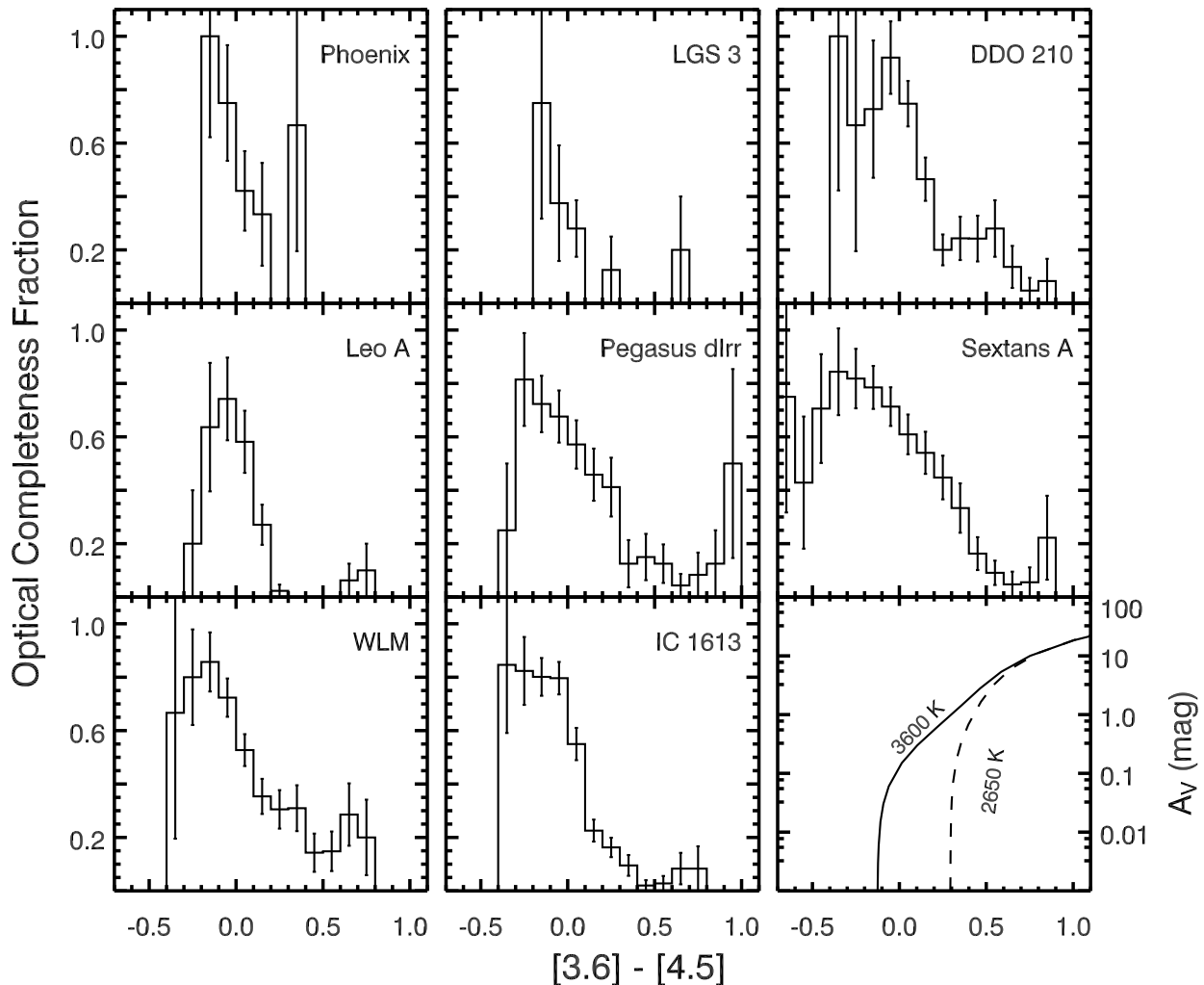


Fig. 14.— Fraction of stars detected in the optical as a function of $[3.6] - [4.5]$. The optical completeness fraction includes only stars detected above the $3.6 \mu\text{m}$ TRGB and the I -band TRGB. The errors bars were determined by taking the square root of the number of optically detected AGB stars and dividing by the total number of IR-identified AGB candidates and therefore only represent the degree to which small-number statistics might affect the trend. The lower right panel shows the visual extinction as a function of $[3.6] - [4.5]$ for a dust composition of 85% AMC and 15% SiC and effective temperatures of 3600 K (solid line) and 2650 K (dashed line). In all eight galaxies, the optical completeness decreases as a function of optical depth, as expected, reaching zero near $[3.6] - [4.5] \approx 0.5$ in most cases. In all galaxies but Sextans A and WLM, there is a secondary dip in completeness near a color of 0.2, which may be due to the presence of background galaxies and indicates that, in these galaxies, there are very few AGB stars redward of this drop-off.

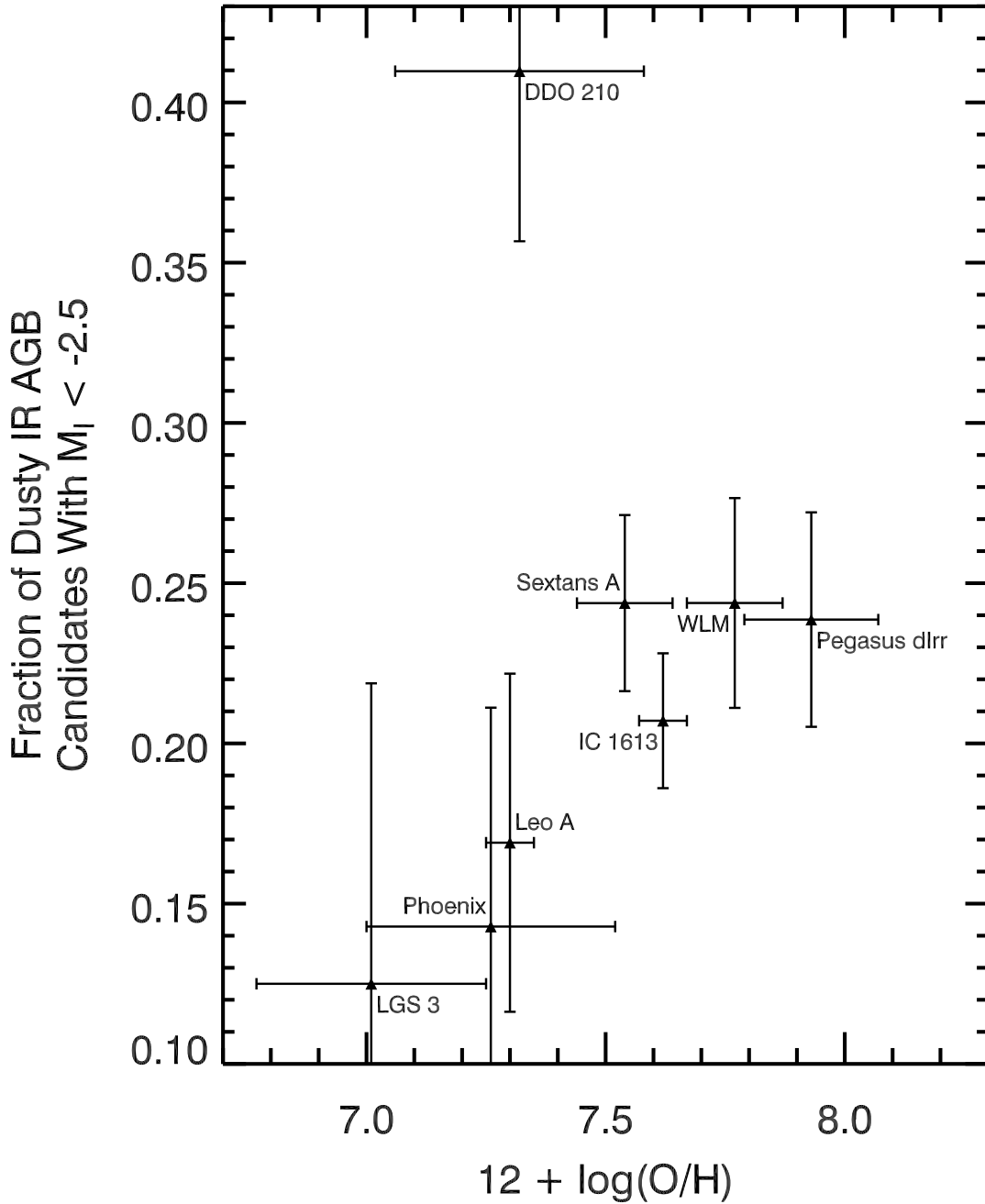


Fig. 15.— Fraction of red stars in each galaxy. The fraction includes only IR AGB candidates that are detected in the optical with $M_I < -2.5$ mag, and therefore does not include the most extreme dusty stars. A source is considered “red” if $[3.6] - [4.5] > 0.2$. With the exception of DDO 210, we see a clear trend for higher metallicity galaxies to have a higher fraction of moderately red stars. This trend may be due to metallicity, but may also be due to the age of the populations.

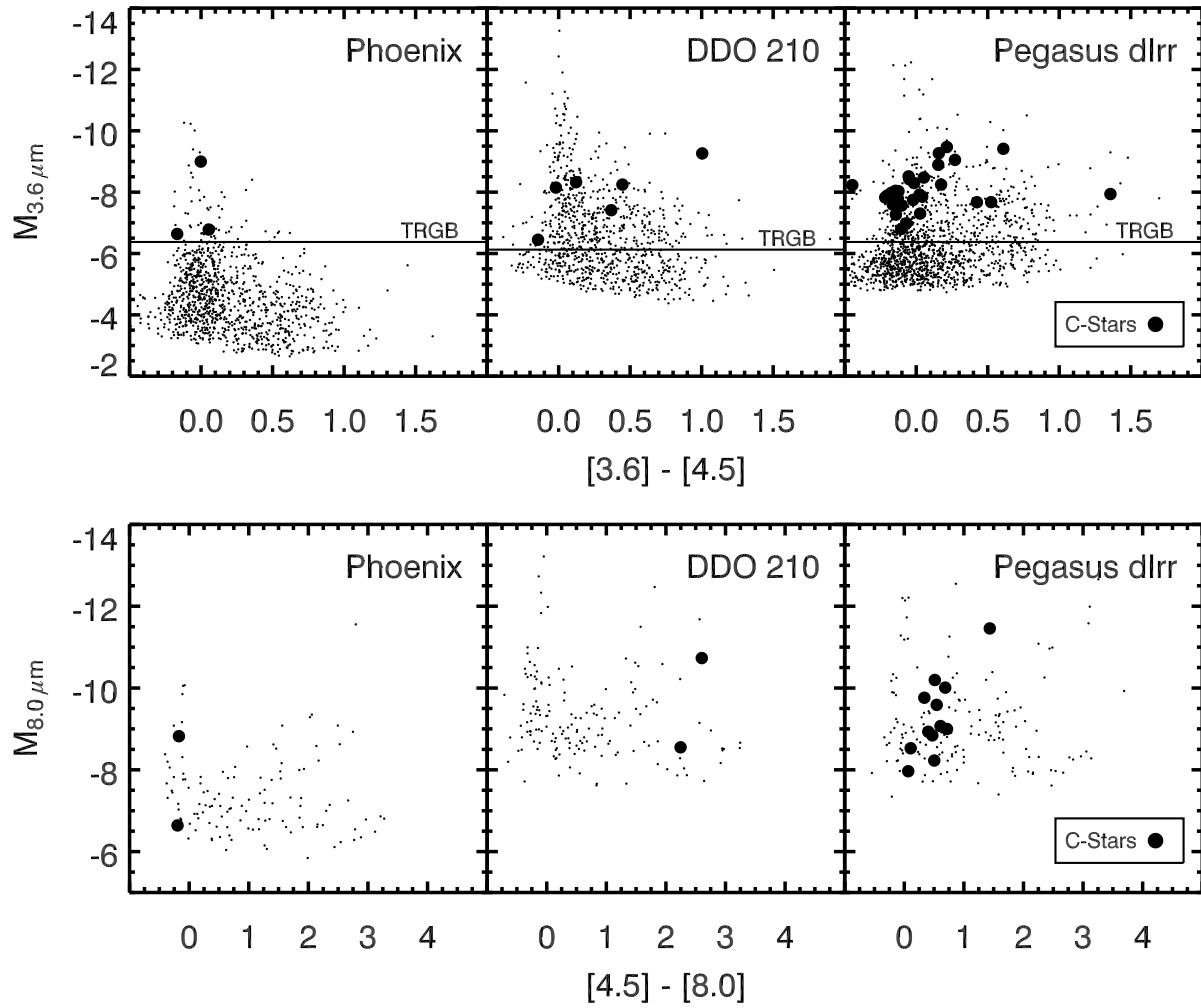


Fig. 16.— Carbon stars on the $[3.6]$ vs. $[3.6] - [4.5]$ and $[8.0]$ vs. $[4.5] - [8.0]$ color magnitude diagrams. The small black dots mark all of the IRAC detections, and the large black circles mark carbon stars identified in Phoenix (Da Costa 1994; Menzies et al. 2008), DDO 210 (Battinelli & Demers 2000), and Pegasus dIrr (Battinelli & Demers 2000). The carbon stars with $[3.6] - [4.5] > 0.2$ are likely losing significant mass.

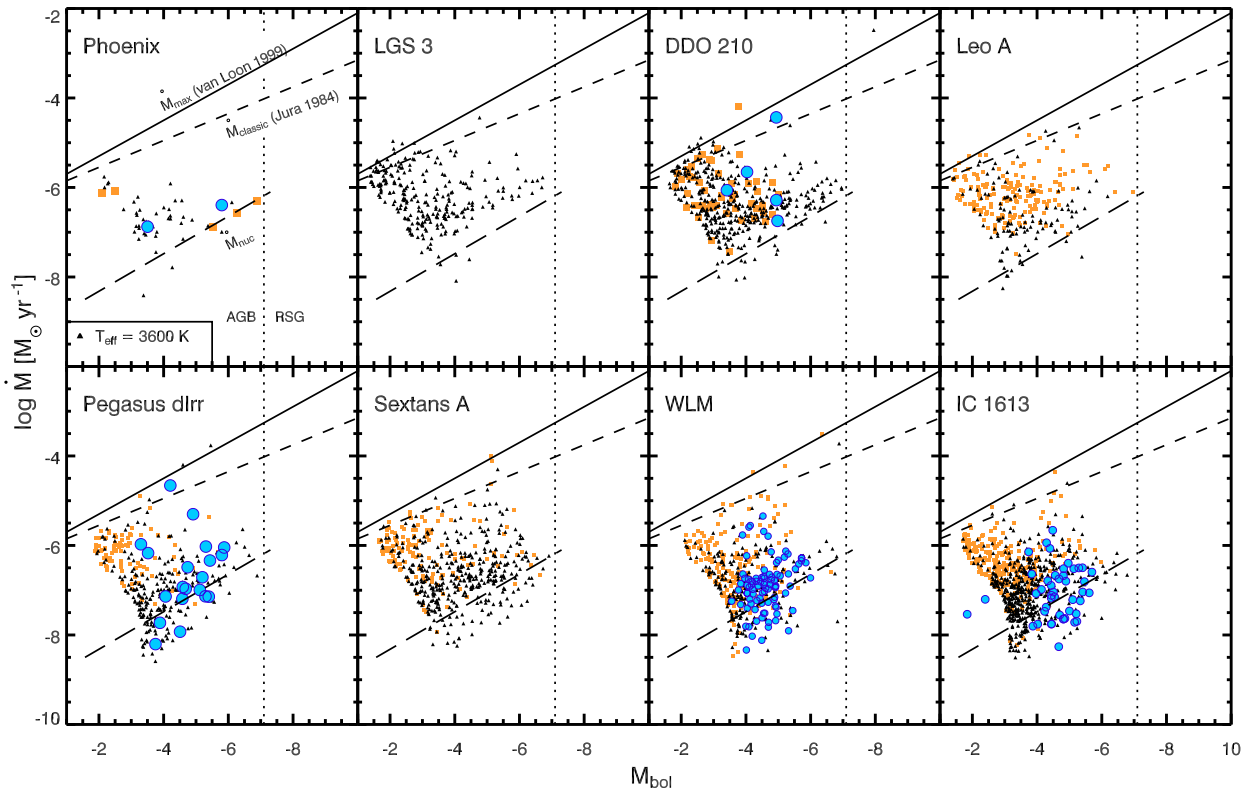


Fig. 17.— Mass-loss rates vs. bolometric magnitudes for all objects brighter than the $3.6 \mu\text{m}$ TRGB, fainter than the AGB limit, and *not* optically identified as an RSG or a blue object. Orange squares are sources with $M_I > -2.5$ mag and $m_{3.6} > 16$ mag and are heavily contaminated with background galaxies. Large blue circles are carbon stars. There are no Orange squares in LGS 3 due to the difficulty in matching IRAC sources to ACS sources (§ 2.3). Mass-loss rates were derived using the Groenewegen (2006) models (§ 4.3), assuming a wind composition of 85% AMC and 15% SiC and an effective temperature of $T_{\text{eff}} = 3600$ K. The short-dashed line marks the classical single-scattering limit from Jura (1984) (\dot{M}_{classic}) and the solid line marks the maximum mass-loss rates (\dot{M}_{max}) observed in the Large Magellanic Cloud (van Loon et al. 1999). The lower, long-dashed line marks the nuclear-burning mass consumption rate (\dot{M}_{nuc}) and the vertical, dotted line marks the AGB limit at $M_{\text{bol}} = -7.1$ mag. Several stars in each galaxy, save Phoenix, are above the single-scattering limit and have large optical depths.

Table 1. Basic Galaxy Properties

Quantity	Phoenix	LGS 3	DDO 210	Leo A	Pegasus dIrr	Sextans A	WLM	IC 1613
Right Ascension $\alpha(\text{J2000})$	01 ^h 51 ^m 06 ^s	01 ^h 03 ^m 57 ^s	20 ^h 46 ^m 52 ^s	09 ^h 59 ^m 27 ^s	23 ^h 28 ^m 36 ^s	10 ^h 11 ^m 01 ^s	00 ^h 01 ^m 58 ^s	01 ^h 0 ^m 45 ^s
Declination $\delta(\text{J2000})$	-44°26'7	+21°53'7	-12°50'9	+30°44'8	+14°44'6	-04°41'5	-15°27'8	+02°08'0
$(m - M)_0$ (mag) ^a	23.24 ± 0.12	24.54 ± 0.15	25.15 ± 0.08 [8]	24.51 ± 0.12 [3]	24.9 ± 0.1	25.61 ± 0.07 [4]	24.81 ± 08 [11]	24.32 ± 0.06 [2]
Morphological Type	dIrr/dSph	dIrr/dSph	dIrr/dSph	dIrr	dIrr/dSph	dIrr	IrrIV-V	IrrV
M_V (mag)	-10.1	-10.35 [9]	-10.6 [10]	-11.4	-12.9	-14.6	-14.5	-14.7
12 + log (O/H) ^b	7.26 ± 0.26	7.01 ± 0.24	7.32 ± 0.26	7.30 ± 0.05	7.93 ± 0.14	7.54 ± 0.10	7.83 ± 0.06	7.62 ± 0.05
Holmberg semiaxes a_H, b_H	0.9', 1.6'	2.3', 3.5'	2.3', 3.9'	3.2', 4.0'	2.2', 5.5'	...
log(M_{HI}) (M_\odot)	6.5 [14]	5.0 [12]	5.3 [12]	7.0 [14]	6.5 [5]	7.9 [1]	7.7 [6]	7.8 [13]
log($M_{\text{Dynamical}}$) (M_\odot)	7.5	7.1	6.7	7.0	7.8	8.6	8.2	8.9

Table 1—Continued

Quantity	Phoenix	LGS 3	DDO 210	Leo A	Pegasus dIrr	Sextans A	WLM	IC 1613
$\log(M_*)$ (M_\odot) ^c ...	5.40	4.56	5.60	5.89	6.98	6.24	6.88	6.82
TRGB _{3.6 μm}} (mag) ^d ..	-6.38 ± 0.25	-5.88 ± 0.25	-6.13 ± 0.25	-6.88 ± 0.25	-6.38 ± 0.25	-6.13 ± 0.25^e	-6.6 ± 0.25	-6.2 ± 0.20

Note. — All values in this table are from Mateo (1998), unless marked otherwise in brackets.

References. — [1] Barnes & de Blok (2004); [2] Dolphin et al. (2001); [3] Dolphin et al. (2002); [4] Dolphin et al. (2003a); [5] Hoffman et al. (1996); [6] Huchtmeier et al. (1981); [7] Mateo (1998); [8] McConnachie et al. (2006); [9] Lee (1995); [10] Lee et al. (1999); [11] Lee et al. (2006); [12] Lo et al. (1993); [13] Volders & Högbom (1961); [14] Young & Lo (1996).

^a Distance modulus.

^b Values of $12 + \log(\text{O}/\text{H})$ for galaxies containing H II regions (Leo A, Pegasus dIrr, and Sextans A) are taken from van Zee et al. (2006). For galaxies without H II regions (Phoenix, LGS 3, and DDO 210), the L - Z relationship determined by Lee et al. (2006) was used to determine $12 + \log(\text{O}/\text{H})$. To compute mass-loss rates, Z was determined using $Z_\odot = 0.0122$ and $12 + \log(\text{O}/\text{H})_\odot = 8.66$ (Asplund et al. 2004).

^c Stellar masses for Leo A, Pegasus dIrr, and Sextans A are taken directly from Lee et al. (2006). For Phoenix, LGS 3, and DDO 210, we used the mass-metallicity relation derived by Lee et al. (2006) with $4.5 \mu\text{m}$ fluxes from Jackson et al. (2006).

^d The $3.6 \mu\text{m}$ TRGBs as determined from this work (see § 3.2), except for WLM (Paper I) and IC 1613 (Paper II).

^e The Sextans A $3.6 \mu\text{m}$ TRGB is not measured from the IRAC data directly, but by plotting the $3.6 \mu\text{m}$ luminosity function of optical sub-TRGB stars (see § 3.2).

Table 2. Observation Details

Galaxy Name	AOR key	α (J2000)	δ	PID	Date (UT)	λ (μm)	Depth (s)
LGS 3	5051393	01:03:52.65	+21:53:00.2	128	2005 Jul 23	4.5, 8.0	968
	23043072	01:03:58.86	+21:49:57.1	40524	2007 Aug 12	3.6, 5.8	965
Phoenix	5052160	01:51:05.65	−44:26:42.0	128	2003 Dec 06	4.5, 8.0	968
	23043328	01:51:04.84	−44:30:02.9	40524	2007 Sep 07	3.6, 5.8	965
Leo A	5052416	09:59:26.23	+30:44:47.8	128	2003 Dec 06	4.5, 8.0	968
	23042816	09:59:26.63	+30:44:47.5	40524	2007 Dec 28	3.6, 5.8	965
Sextans A	5053696	10:11:06.45	−04:38:27.9	128	2003 Dec 06	4.5, 8.0	968
	15892224	10:10:55.20	−04:44:38.6	128	2005 Dec 24	3.6, 5.8	858
DDO 210	5054976	20:46:51.70	−12:50:47.0	128	2004 Oct 09	4.5, 8.0	968
	23043328	20:46:52.01	−12:50:51.2	40524	2007 Nov 13	3.6, 5.8	965
Pegasus dIrr	5055744	23:28:36.16	+14:44:35.1	128	2004 Jul 26	4.5, 8.0	968
	23043840	23:28:44.24	+14:41:49.6	40524	2007 Aug 16	3.6, 5.8	965

Table 3. Sample Table: IRAC Point-Source Magnitudes

Galaxy	Source ID	Apparent Magnitude			
		3.6 μm	4.5 μm	5.8 μm	8.0 μm
Phoenix	SSTU J015043.49–442657.4	...	18.7±0.2	...	16.6±0.2
Phoenix	SSTU J015044.85–442653.7	...	17.8±0.1	...	16.7±0.3
Phoenix	SSTU J015046.46–442618.3	...	18.7±0.2	...	16.0±0.2
Phoenix	SSTU J015047.39–442634.8	...	17.0±0.1	...	15.5±0.1
Phoenix	SSTU J015047.77–442624.4	...	19.9±0.5	...	16.8±0.3
Phoenix	SSTU J015049.42–442835.3	16.8±0.1	...	16.3±0.1	...
Phoenix	SSTU J015049.43–442739.9	19.7±0.3	19.1±0.2
Phoenix	SSTU J015049.57–442551.3	...	19.7±0.4	...	17.0±0.4
Phoenix	SSTU J015049.70–442729.4	19.1±0.2	19.2±0.2
Phoenix	SSTU J015049.85–442753.1	19.4±0.2	18.6±0.3	17.3±0.2	...

Note. — The full version of this table includes the IRAC photometry for all eight galaxies and is available electronically. The source ID follows the standard *Spitzer* naming convention, giving the truncated (J2000) coordinates.

Table 4. Nearby background Galaxy Clusters

dIrr Galaxy	Cluster Name	Angular Distance ^a	Angular Cluster Radius	Cluster Population (No. Galaxies)
LGS 3	Zwicky 317	20'	16.2'	64
	Zwicky 337	43'	9'	66
Leo A	Zwicky 2776	15'	7'	90
	Zwicky 2778	22'	13'	107
	Zwicky 2827	40'	16'	123
	Zwicky 2813	50'	7'	76
	Zwicky 2866	58'	6'	77
Pegasus dIrr	Zwicky 8949	60'	8'	57
	Zwicky 8933	60'	58'	352
WLM	CEDAG 12	26'	...	50 – 80
	CEDAG 10405	26'	...	80 – 130
IC 1613	Zwicky 336	25'	13'	114
	CEDAG 461	55'	...	30 – 40

Note. — Galaxy clusters within one degree of our targets are listed here (Abell 1995; Fernandez et al. 1996).

^a Projected angular distance of the dIrr galaxy from the center of the background galaxy cluster.

Table 5. Detection Statistics

Total Point-Source 4σ Detections in All Wavebands								
Filter	Phoenix	LGS 3	DDO 210	Leo A	Pegasus dIrr	Sextans A	WLM	IC 1613
	(Number)							
Both V and I	2026	369	1532	2525	2251	2968	4896	7574
$3.6\ \mu\text{m}$	1087	283	907	778	1422	1162	2855	5556
$4.5\ \mu\text{m}$	1061	285	893	784	1369	1204	2019	3362
$5.8\ \mu\text{m}$	462	49	326	261	451	360	300	998
$8.0\ \mu\text{m}$	107	50	184	148	204	283	122	696
4σ Detections in All Four IRAC Bands, But Not V and I								
Object Type	(Number)							
Total.....	40	...	27	63	67	66	46	190
Above AGB limit.....	1	...	3	3	5	11	3	4
Above TRGB, below AGB limit.....	14	...	22	60	58	55	42	183
Below TRGB.....	25	...	2	0	4	0	1	6
3.6 μm Point-Source Flux								
Total Flux (mJy).....	19.6	13.0	22.9	19.6	23.9	26.9	40.1	74.0
Average 3.6 μm flux (mJy arcmin $^{-2}$)	0.6	0.4	0.7	0.6	0.7	0.8	1.2	2.2
Flux 1 mag Above/Below TRGB ^a ..	0.60	1.59	1.78	1.36	1.11	3.30	1.41	1.13
$f_{1\ \text{Gyr}}$ (Orban et al. 2008) ^b	0.027	0.015	0.037	0.13	0.057	0.15	0.14	0.059

Note. — Numbers in this table are computed only for areas where the IRAC and optical coverage overlaps. Some entries for LGS 3 are left blank due to the difficulty of matching IRAC data with the high-resolution HST data (§ 2.3). Stars brighter than

the *I*-band TRGB in LGS 3 were matched to their IR counterparts by eye. See Papers I and II for similar tables for WLM and IC 1613.

^a The ratio of the cumulative flux one magnitude brighter than (above) to one magnitude fainter than (below) the $3.6 \mu\text{m}$. The uncertainty of this quantity ranges from 5% to 18%.

^b The fraction of the total stellar mass that has been formed within the last 1 Gyr (Orban et al. 2008).

Table 6. Detection Statistics of IR-Identified AGB Candidates

	Phoenix	LGS 3	DDO 210	Leo A	Pegasus dIrr	Sextans A	WLM ^a	IC 1613 ^a
No. IR AGB candidates ^b	57	102	447	302	422	673	612	956
No. foreground stars ^c ...	6	10	32	6	10	10	9	15
No. background galaxies ^d	20	68	287	180	105	195	161	362
No. known carbon stars ^e	3	0	7	0	32	0	100	70
IR AGB Candidates Detected With:								
$M_I < -2.5$ mag.....	68%	...	64%	28%	56%	55%	58%	54%
$M_I < I$ -band TRGB.....	44%	12%	40%	21%	52%	54%	46%	49%
Corrected ^f	84%	50%	140%	54%	72%	78%	64%	81%
Stellar Mass Derived from IR AGB Candidates:								
$\log(M_{2Gyr}^*) (M_\odot)^g$	5.74	6.20	6.51	6.36	6.64	6.77	6.85	7.07
$\log(M_{SFH}^*) (M_\odot)^h$	5.20 – 5.74	5.75 – 6.20	5.92 – 6.81	5.77 – 5.91	6.19 – 6.94	6.17 – 6.20	6.40 – 6.85	6.62 – 7.374
$\log(M_*) (M_\odot)^i$	5.40	4.56	5.60	5.89	6.98	6.24	6.88	6.82

Note. — Numbers in this table are computed only for areas where the IRAC and optical coverage overlaps. Some entries for LGS 3 are left blank due to the difficulty of matching IRAC data with the high-resolution HST data (§ 2.3). Stars brighter than the I -band TRGB in LGS 3 were matched to their IR counterparts by eye.

^a Similar quantities are presented for WLM in Paper I and for IC 1613 in Paper II. We present updated values here for these two galaxies using the same analysis procedure used for the six new galaxies in the sample.

^b IR-identified AGB candidates are those between the $3.6 \mu\text{m}$ TRGB and the AGB limit that are not identified as either a blue object or an RSG in the optical (§ 4). This quantity includes contamination from background galaxies and foreground stars, also listed in this Table.

^c Estimated number of foreground stars from Robin et al. (2003).

^d Estimated number of unresolved background galaxies above the $3.6 \mu\text{m}$ TRGB found through fitting the radial profiles of AGB candidates (see § 3.4). These estimates are within 25% of the estimates measured from S-COSMOS data for four galaxies, 40% for three, and 78% for

IC 1613.

^e Carbon stars listed are those detected in IRAC. The carbon star searches were carried out by: Battinelli & Demers (2000) for DDO 210 and Pegasus dIrr, Da Costa (1994) and Menzies et al. (2008) for Phoenix, Battinelli & Demers (2004) for WLM, and Albert et al. (2000) for IC 1613.

^f IR AGB candidates detected with $M_I < I$ -band TRGB, with subtraction of foreground stars and unresolved background galaxies from radial profile fitting (see § 3.4).

^g Total stellar mass (M_{2Gyr}^*) was determined following van Loon et al. (2005), assuming an age of 2 Gyr, and using the number of $3.6 \mu\text{m}$ stars above the TRGB, excluding estimates of the numbers of background galaxies from S-COSMOS and foreground stars from Robin et al. (2003).

^h Total stellar mass (M_{SFH}^*) was determined following van Loon et al. (2005), assuming a single age range based on past star formation events (Dolphin et al. 2005), and using the number of $3.6 \mu\text{m}$ stars above the TRGB, excluding estimates of the numbers of background galaxies from S-COSMOS and foreground stars from Robin et al. (2003).

ⁱ Total stellar mass from Table 1.

Table 7. Average Stellar Mass-Loss Rates

All IR Sources With $M_{3.6} < \text{TRGB}$ ($10^{-6} M_{\odot} \text{ yr}^{-1}$)					
Galaxy	C-rich 1 ^a	C-rich 2 ^b	O-rich 1 ^c	O-rich 2 ^d	O-rich 3 ^e
Phoenix	0.53	0.31	1.4	1.2	1.1
LGS 3	2.21	1.4	5.4	4.6	4.6
DDO 210	2.7	1.4	5.8	4.9	4.6
Leo A	1.6	1.2	4.0	3.4	3.7
Pegasus dIrr	2.1	0.88	4.4	3.9	2.6
Sextans A	2.4	1.2	5.4	4.5	3.6
WLM	3.5	1.1	6.6	5.7	3.5
IC 1613	1.1	0.47	2.1	1.8	1.5

Note. — The mass-loss rates quoted here include only sources located between the $3.6 \mu\text{m}$ TRGB and the AGB limit that are not optically identified as a blue object or RSG. Due to color limits in the Groenewegen (2006) models, C-rich 2 and O-rich 1 include the most sources, while C-rich 1 includes the fewest.

^a C-rich AGB star, $T_{\text{eff}} = 2650 \text{ K}$, dust composition is 85% amorphous carbon, 15% SiC.

^b C-rich AGB star, $T_{\text{eff}} = 3600 \text{ K}$, dust composition is 85% amorphous carbon, 15% SiC.

^c O-rich AGB star, $T_{\text{eff}} = 2500 \text{ K}$, dust composition is 60% silicates, 40% aluminum oxides.

^d O-rich AGB star, $T_{\text{eff}} = 2500 \text{ K}$, dust composition is 100% silicates.

^e O-rich AGB star, $T_{\text{eff}} = 3300 \text{ K}$, dust composition is 60% silicates, 40% aluminum oxides.

Table 8. Integrated Galaxy Mass-Loss Rates

All AGB Candidates ($M_{3.6} < \text{TRGB}; 10^{-4} M_{\odot} \text{ yr}^{-1}$)					
Galaxy	C-rich 1 ^a	C-rich 2 ^a	O-rich 1 ^a	O-rich 2 ^a	O-rich 3 ^a
Phoenix	0.05	0.18	0.29	0.25	0.65
LGS 3	2.4	3.7	9.5	7.9	12
DDO 210	39	39	75	94	76
Leo A	2.0	3.3	8.6	7.3	11
Pegasus dIrr	4.1	4.7	12	12	13
Sextans A	5.0	6.9	19	16	23
WLM	7.8	9.2	25	23	28
IC 1613	2.4	4.2	10	8.8	14

All AGB Candidates With $M_{\text{I}} < -2.5$ ($10^{-4} M_{\odot} \text{ yr}^{-1}$)					
Phoenix	0.03	0.11	0.15	0.13	0.20
LGS 3
DDO 210	1.1	2.3	5.0	4.3	8.0
Leo A	0.57	0.82	2.0	1.6	2.6
Pegasus dIrr	3.3	3.7	9.3	9.2	10
Sextans A	1.6	2.8	6.9	5.7	9.5
WLM	2.2	2.8	8.0	6.9	9.5
IC 1613	0.67	1.6	3.4	2.9	5.7

All AGB Candidates With $M_{\text{I}} < -2.5$ Or With $m_{3.6} < 16$ ($10^{-4} M_{\odot} \text{ yr}^{-1}$)					
Phoenix	0.03	0.12	0.15	0.13	0.44
LGS 3
DDO 210	1.5	2.7	6.1	5.2	9.2
Leo A	0.94	1.5	3.7	3.1	4.8
Pegasus dIrr	3.3	3.8	9.4	9.4	10
Sextans A	1.6	2.8	7.1	5.9	9.8
WLM	3.4	4.2	12	10	14
IC 1613	1.2	2.3	5.3	4.5	8.0

All AGB Candidates Minus the No. Galaxies Times the Average Stellar MLR ($10^{-4} M_{\odot} \text{ yr}^{-1}$) ^b					
Phoenix	0.0	0.11	0.04	0.03	0.42
LGS 3	0.11	1.4	0.84	0.71	4.7
DDO 210	0.25	3.2	4.0	3.4	11
Leo A	0.38	1.5	2.5	2.1	5.1
Pegasus dIrr	0.38	1.8	2.1	1.8	5.9
Sextans A	0.0	2.5	0.13	0.11	9.2
WLM	1.2	4.3	6.6	5.7	15
IC 1613	0.64	2.8	4.8	4.0	9.6

Note. — The mass-loss rates quoted here include only stars located between the $3.6 \mu\text{m}$ TRGB and the AGB limit that are not optically identified as a blue object or RSG. Due to color limits in the Groenewegen (2006) models, C-rich 2 and O-rich 1 include the most sources, while C-rich 1 includes the fewest.

^aSee Table 7 for descriptions of these labels.

^bThe number of galaxies here were estimated from S-Cosmos data.

Table 9. ISM Gas Return

Galaxy	$\dot{M}_{\text{dusty}}^{\text{a}}$ ($M_{\odot} \text{ yr}^{-1}$)	$\text{SFR}_{(1 \text{ Gyr})}^{\text{b}}$ ($M_{\odot} \text{ yr}^{-1}$)	$\text{SFR}_{(5 \text{ Gyr})}^{\text{b}}$ ($M_{\odot} \text{ yr}^{-1}$)	$f_{\text{return}}^{\text{c}}$	$\tau_{\text{R}}^{\text{d}}$ (Gyr)	$\tau_{\text{R,corrected}}^{\text{d}}$ (Gyr)	$\tau_{\text{lifetime}}^{\text{e}}$ (Gyr)	$\tau_{\text{age}}^{\text{b}}$ (Gyr)
Phoenix	1.2×10^{-5}	5.4×10^{-5}	9.2×10^{-5}	0.22	59	76	43	10.3
LGS 3	1.6×10^{-4}	3.0×10^{-5}	6.4×10^{-5}	5.30	3.3	9.8
DDO 210	4.4×10^{-4}	1.9×10^{-4}	1.2×10^{-4}	2.32	1.1	12.0
Leo A	2.3×10^{-4}	8.2×10^{-4}	8.2×10^{-4}	0.24	12	17	18	6.2
Pegasus dIrr	2.4×10^{-4}	8.0×10^{-4}	1.3×10^{-3}	0.30	3.5	4.8	12	7.4
Sextans A	2.4×10^{-4}	1.2×10^{-2}	6.0×10^{-3}	0.02	6.6	6.8	14	9.3
WLM	6.6×10^{-4}	2.2×10^{-2}	1.7×10^{-2}	0.03	2.4	2.5	3.7	6.7
IC 1613	4.4×10^{-4}	1.2×10^{-2}	1.7×10^{-2}	0.04	5.5	5.7	4.3	7.7

Note. — An empty entry indicates an indefinite timescale.

^a \dot{M}_{dusty} is the MLR from the bottom panel of Table 8, averaged over all compositions.

^bAverage SFRs and the mean mass-weighted stellar age (τ_{age}) are from Orban et al. (2008).

^c $f_{\text{return}} = \dot{M}_{\text{dusty}} / \text{SFR}_{(1 \text{ Gyr})}$.

^d τ_{R} is the Roberts Time: $\tau_{\text{R}} = M_{\text{gas}} / \text{SFR}_{(1 \text{ Gyr})}$. The correction factor (recycling factor) for τ_{R} is $(1 - \dot{M}_{\text{dusty}} / \text{SFR}_{(1 \text{ Gyr})})^{-1}$.

^e τ_{lifetime} is the expected total gas-rich lifetime of a galaxy assuming a total initial mass that includes the stellar and H I mass, that the current dusty MLR has remained constant, and that the 5 Gyr average SFR represents the lifetime average SFR: $\tau_{\text{lifetime}} = M_{\text{Total}} / (\text{SFR}_{(5 \text{ Gyr})} - \dot{M}_{\text{dusty}})$.